A Multiplexed Impedance Analyser for Biosensing Applications

Karl Voigt

24867209

Report submitted in partial fulfilment of the requirements of the module
Project (E) 448 for the degree Baccalaureus in Engineering in the Department of
Electrical and Electronic Engineering at Stellenbosch University.

Supervisor: Dr T. Ebrahim

October 2025

Acknowledgements

I would like to thank my dog, Muffin. I also would like to thank the inventor of the incubator; without him/her, I would not be here. Finally, I would like to thank Dr Herman Kamper for this amazing report template.

Plagiaatverklaring / *Plagiarism Declaration*

1. Plagiaat is die oorneem en gebruik van die idees, materiaal en ander intellektuele eiendom van ander persone asof dit jou eie werk is.

   Plagiarism is the use of ideas, material and other intellectual property of another's work and to present is as my own.

2. Ek erken dat die pleeg van plagiaat 'n strafbare oortreding is aangesien dit 'n vorm van diefstal is.

   I agree that plagiarism is a punishable offence because it constitutes theft.

3. Ek verstaan ook dat direkte vertalings plagiaat is.

   I also understand that direct translations are plagiarism.

4. Dienooreenkomstig is alle aanhalings en bydraes vanuit enige bron (ingesluit die internet) volledig verwys (erken). Ek erken dat die woordelikse aanhaal van teks sonder aanhalingstekens (selfs al word die bron volledig erken) plagiaat is.

   Accordingly all quotations and contributions from any source whatsoever (including the internet) have been cited fully. I understand that the reproduction of text without quotation marks (even when the source is cited) is plagiarism

5. Ek verklaar dat die werk in hierdie skryfstuk vervat, behalwe waar anders aangedui, my eie oorspronklike werk is en dat ek dit nie vantevore in die geheel of gedeeltelik ingehandig het vir bepunting in hierdie module/werkstuk of 'n ander module/werkstuk nie.

   I declare that the work contained in this assignment, except where otherwise stated, is my original work and that I have not previously (in its entirety or in part) submitted it for grading in this module/assignment or another module/assignment.

Studentenommer / *Student number*	Handtekening / *Signature*
Voorletters en van / *Initials and surname*	Datum / *Date*

Abstract

English

The English abstract.

Afrikaans

Die Afrikaanse uittreksel.

Contents

List of Figures

List of Tables

Nomenclature

Variables and functions

$p(x)$	Probability density function with respect to variable x.
$P(A)$	Probability of event A occurring.
ε	The Bayes error.
ε_u	The Bhattacharyya bound.
B	The Bhattacharyya distance.
s	An HMM state. A subscript is used to refer to a particular state, e.g. s_i refers to the ith state of an HMM.
$\mathbf{S}$	A set of HMM states.
$\mathbf{F}$	A set of frames.
$\mathbf{o}_f$	Observation (feature) vector associated with frame f.
$\gamma_s(\mathbf{o}_f)$	A posteriori probability of the observation vector $\mathbf{o}_f$ being generated by HMM state s.
μ	Statistical mean vector.
Σ	Statistical covariance matrix.
$L(\mathbf{S})$	Log likelihood of the set of HMM states $\mathbf{S}$ generating the training set observation vectors assigned to the states in that set.
$\mathcal{N}(\mathbf{x}|\mu, \Sigma)$	Multivariate Gaussian PDF with mean μ and covariance matrix Σ.
a_{ij}	The probability of a transition from HMM state s_i to state s_j.
N	Total number of frames or number of tokens, depending on the context.
D	Number of deletion errors.
I	Number of insertion errors.
S	Number of substitution errors.

Acronyms and abbreviations

ADC analogue-to-digital converter

BLE Bluetooth Low Energy

CPE constant phase element

DAC digital-to-analogue converter

DMA direct memory access

DSP digital signal processing

DUT device-under-test

EIS electrochemical impedance spectroscopy

EMI electromagnetic interference

FFT fast Fourier transform

FPU floating point unit

GBW gain-bandwidth product

LPF low-pass filter

MCU microcontroller unit

MUX multiplexer

PGA programmable gain amplifier

POC point-of-care

TIA transimpedance amplifier

Chapter 1

Introduction

1.1. Background

Biosensors are defined as devices that measures biological and chemical reactions through the use of a physical transducer mechanism which in turn generates signals porportional to the concentration of an analyte in a sample. [4] This allows for the detection of various biological elements such as biomarkers which can be used to monitor health conditions or diagnose diseases.

Designing a low-cost easy to use device to take readings from biosensors, would thus provide a valuable tool for the early screening of diseases such as cancer. Changing wording and goals to be focused on point of care screening rather than analysis/detection

This would decrease the need for expensive labratory testing and allow for lower cost and more regular testing of patients using a point-of-care device. Having a multiplexed device, able to take readings from multiple biosensors, would allow a single blood sample to be taken and multiple tests to be run on it with minimum involvement from a healthcare professional.

1.2. Project Objectives

This is a multifaceted project that aims to develop a low-cost, easy-to-use device for reading biosensors. The system design objectives for the device include:

- Developing a circuit that allows a microcontroller to read a biosensor through the use of Electrochemical Impedance Spectroscopy (EIS). This entails conditioning the sinusoidal signal generated by a DAC and measuring the current response from the biosensor through an ADC.

- This measurement circuitry needs to be multiplexed to allow for multiple biosensors to be read in turn without the need for human intervention.

- The microcontroller should be able to filter and process the biosensor data to determine the concentration of the analyte in the sample.

- The device needs to be able to communicate these results in a clear and user-friendly manner. This will be done through the use of a LCD screen on the device as well as a web interface that can be accessed through a smartphone or computer.

- The device should be battery powered, low-cost and easy to use, thus allowing for widespread adoption and use in various environments.

1.3. Project Scope

NOT THE DESIGN OF Biosensors NOT TESTING WITH REAL BLOOD (We arent qualified for that)

1.4. Chapter Overview

Chapter 1: Introduction
Provides an overview of the motivation, background, objectives, scope, and structure of the report.

Chapter 2: Literature Review
Reviews relevant research and technologies in speech recognition and neural networks.

Chapter 3: Methodology
Describes the methods and approaches used in the project, including data collection and model development.

Chapter 4: Experiments and Results
Presents experimental setup, results, and analysis.

Chapter 5: Discussion
Discusses findings, limitations, and implications of the results.

Chapter 6: Conclusion and Future Work
Summarizes the work and suggests directions for future research.

Chapter 2

Literature Review

2.1. Biosensors

Biosensors are employed in applications such as disease monitoring, drug discovery, and detection of pollutants, disease-causing micro-organisms and markers that are indicators of a disease in bodily fluids (blood, urine, saliva, sweat). [4]

2.1.1. Background on Biomarkers

A biomarker is an objective measure that that gives an indication of the biological processes happening inside the body at a given moment. [5] They are physical substances found in the body that can be measured. The concentration of biomarkers differs between healthy individuals and individuals with diseases, thereby aiding in diagnosis and monitoring of diseases. [6] Some biomarkers are easy to measure (such as blood pressure, body weight, etc.) while others require tests of blood, urine or tissue samples. [5]

This project will focus on the detection of biomarkers found in blood samples such as the CA-19 biomarker used for pancreatic cancer detection. Note: Verduidelik bietjie oor CA-19. The concentration of these biomarkers in blood can give an indication of the presence and progression of a variety of diseases, including many types of cancer. [7]

2.1.2. Types of Biosensors

A biosensor consists of an analyte, a bioreceptor and a transducer mechanism combined with the electronics needed to process the signal. [4] The analyte is the substance of interest (such as biomarkers) that needs detection. Bioreceptors are molecules such as enzymes, cells, DNA or antibodies that specifically recognise the analyte. These bioreceptors produce a signal (in the form of light, heat, pH, charge or mass change, etc.) when they interact with the analyte. [4] Antibody based biosensors are the type of biosensor that will be used to detect biomarkers in this project.

Antibodies are produced by vertebrates as part of their immune response to foreign organisms or substances (called antigens). They are the most common biorecognition element used in biosensors. [8] Antibodies are Y-shaped cells that can be divided into two

distinct regions. The top of the Y is variable and binds to a specific antigen depending on the amino acids present in this region. The amino acids present in the constant region (the bottom of the Y) is similar between different classes of antibodies (within the same species of animal). [8] This constant region binds to the substrate of the biosensor during immobilization, leaving the variable region free to bind with antigens. [9]
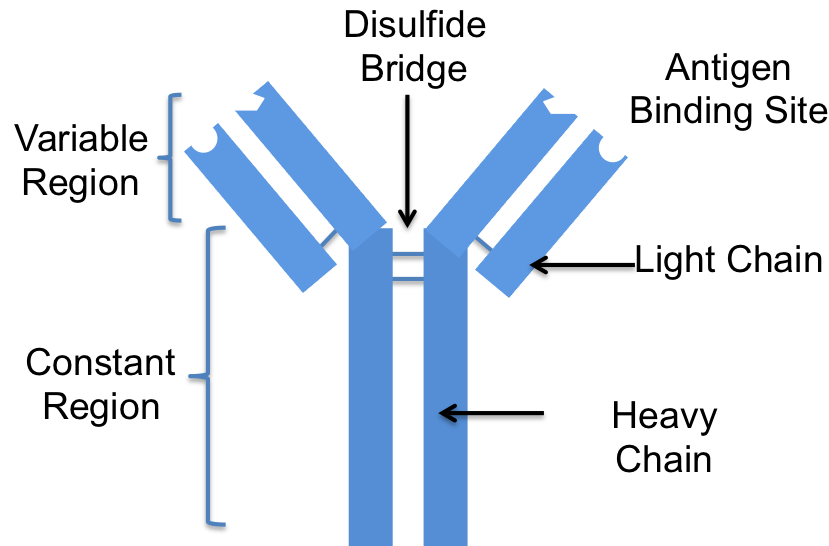
Figure 2.1: Antibody with basic structural features labeled [10]

Many biosensors require that a "label" is attached to the biomolecule of interest and then the concentration of this label is detected and extrapolated to the concentration of the biomolecule [11]. Label-free biosensors, on the other hand, directly detect the target biomolecule by measuring the changes in electrical properties of the surface of the biosensor when binding occurs. Since labeling can dramatically alter the binding properties of biomolecules and adds complexity and cost to the assay process, label-free detection is highly desirable [11], especially in point-of-care environments.

2.2. Transducer Mechanisms

The number of biological binding events indicates the concentration of the analyte in the sample. In order to convert the bio-recognition event into a measurable signal, a transducer mechanism is needed [4]. There are various types of transducer mechanisms that can be used in biosensors, including optical, piezoelectric and electrochemical transducers. This project will focus on biosensors where binding events change the electrical properties of the biosensor, specifically the complex impedance. Thus, electrochemical transducers are of interest.

Electrochemical transducers can use various analysis techniques. In potentiometric analysis, the potential of an electrode is measured against a reference electrode at zero-current [12]. Coulometry applies a constant potential (with regards to a reference electrode)

onto an electrode surface to carry out exhaustive electrolysis of an analyte [12]. Voltammetry involves subjecting the sample to a varying potential at the electrode's surface and measuring the resulting Faradaic current [12]. Finally there is electrochemical impedance spectroscopy (EIS), which measures the complex impedance of an electrochemical system as a function of frequency [12]. EIS is particularly suitable for biosensor applications where biological binding events alter the electrical properties of the electrode-electrolyte interface [11].

2.2.1. Electrochemical Impedance Spectroscopy (EIS)

EIS involves applying a small sinusoidal perturbation to the device-under-test (DUT) and measuring the response. This can be either a voltage or current signal, while the other is measured. By varying the frequency of the excitation signal, different electrochemical processes that occur at distinct time constants can be characterised.

EIS relies on the system acting as a linear time-invariant system, but most real-world electrochemical systems are inherently nonlinear [13]. To approximate linear behaviour and ensure valid results, EIS uses a small AC excitation signal, typically between 1–10 mVpp [14] [13]. At higher amplitudes, the response deviates from ideal sinusoidal form, causing harmonic distortion and invalid measurements. However, making the excitation too small reduces signal-to-noise ratio, so 10 mVpp is commonly used to balance linearity and measurement quality. A key advantage of EIS is the ability to simulate the electrochemical system using equivalent circuit models. These models represent the various resistive, capacitive, and diffusive elements that represent the behaviour of the system [13]. This is due to the frequency domain nature of EIS, in comparison with other techniques such as voltammetry that works in the time-domain, thus allowing the behaviour of distinct processes that dominate at certain frequencies to be characterised [13]. By fitting experimental impedance data to these models, parameters such as charge transfer resistance and double-layer capacitance can be extracted, which correlate with biomolecular interactions occurring on the electrode surface [11]. This capability makes EIS a powerful tool for label-free biosensing applications.

2.2.2. Faradaic vs Non-Faradaic EIS Sensors

EIS biosensors can be categorized into two main types based on their transduction mechanism: faradaic and non-faradaic sensors.

In faradaic measurements, charge transfers occur at the electrode-solution interface and redox reactions occur on the electrode surface [15]. The equivalent circuit model for faradaic sensors is the Randles circuit (Figure 2.2a), consisting of solution resistance (R_s) in series with the parallel combination of charge transfer resistance (R_{CT}) and double-layer capacitance (C_{dl}), plus Warburg impedance (Z_w) representing diffusion processes [15].

Non-faradaic measurements operate without charge-transfer reactions, functioning as capacitive sensors that detect changes in the electrical double layer capacitance. Due to the lack of charge-transfer, R_{CT} becomes infinitely large, thus creating an open circuit [15]. On solid electrodes, the observed impedance response of C_{DL} differs from an ideal capacitor, thus a constant phase element (CPE) is used instead of C_{DL} in the Randles non-fardaic equivalent circuit (Figure 2.2b).

(a) Faradaic Randles Circuit   **(b)** Non-Faradaic Randles Circuit
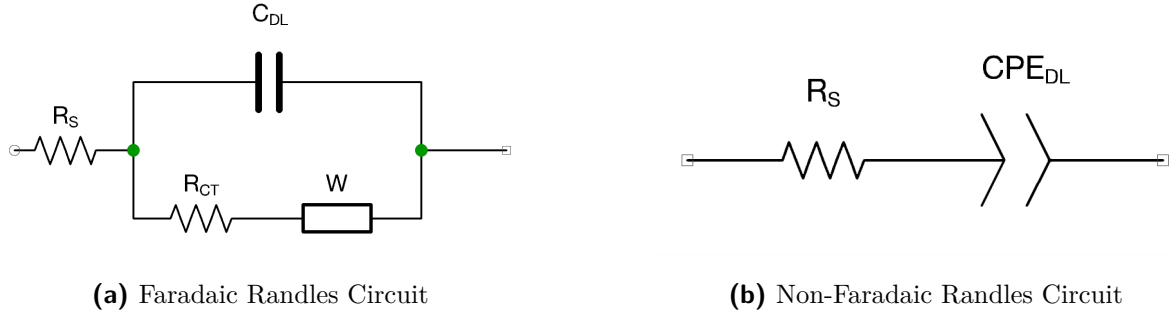
Figure 2.2: Equivalent Circuits for Faradaic and Non-Faradaic EIS Biosensors

2.3. Complex Impedance

Electrochemical impedance spectroscopy (EIS) produces complex impedance data consisting of both magnitude and phase information across a range of frequencies. The complex impedance is calculated as:

$$Z(\omega) = \frac{V(\omega)}{I(\omega)} = Z'(\omega) + jZ''(\omega) \tag{2.1}$$

where $Z'(\omega)$ is the real component representing resistive behaviour and $Z''(\omega)$ is the imaginary component representing capacitive or inductive behaviour (with $V(\omega)$ and $I(\omega)$ representing the phasor voltage and current respectively) [13].

Two major ways of visualizing this complex impedance are the Nyquist and Bode representations, each highlighting different aspects of the electrochemical response.

2.3.1. Nyquist Plot

A Nyquist plot displays the negative imaginary part of impedance($Z''(\omega)$) versus the real part ($Z'(\omega)$) [16]. Each point on the plot corresponds to a particular frequency, though the frequency is not explicitly shown along the axes. For biosensing, high-frequency data points are located near the origin (low impedance), while low-frequency points are farther along the curve (high impedance). The Nyquist plot has the distinct advantage that some circuit parameters can be read directly form the plot [16].

A purely resistive impedance is represented as a point on the x-axis, as it has no imaginary component and is not frequency dependent. A purely capacitive impedance on the other hand is represented as a straight vertical line on the y-axis, as it has no real component and its imaginary component varies inversely with frequency [16]. The series combination of resistive and capacitive elements, thus result in a vertical line offset from the y-axis. The parallel combination of resistive and capacitive elements, however result in a semicircular arc, as current flows though the path of least resistance [16]. At low frequencies, the capacitor acts as an open circuit resulting in the x-axis intercept (or diameter of the semi-circle) representing the magnitude of the resistive elements in the circuit.

For simple electrochemical systems such as a Randles cell, the Nyquist plot appears as a semicircle (frequencies where charge transfer phenomena dominate) ending in a straight line tail (frequencies where mass transfer phenomena dominate) (Figure 2.3) [13]. The series resistance (R_s) can be read directly from the x-axis intercept at high frequencies (closer to the origin), while the charge transfer resistance (R_{CT}) is given by the diameter of the semicircle in middle frequencies. At low frequencies, the Warburg impedance (Z_w) manifests as a 45-degree line due to diffusion-limited processes [13], explaining the observed tail.

(a) Faradaic Randles Circuit [13]

(b) Non-Faradaic Randles Circuit [15]
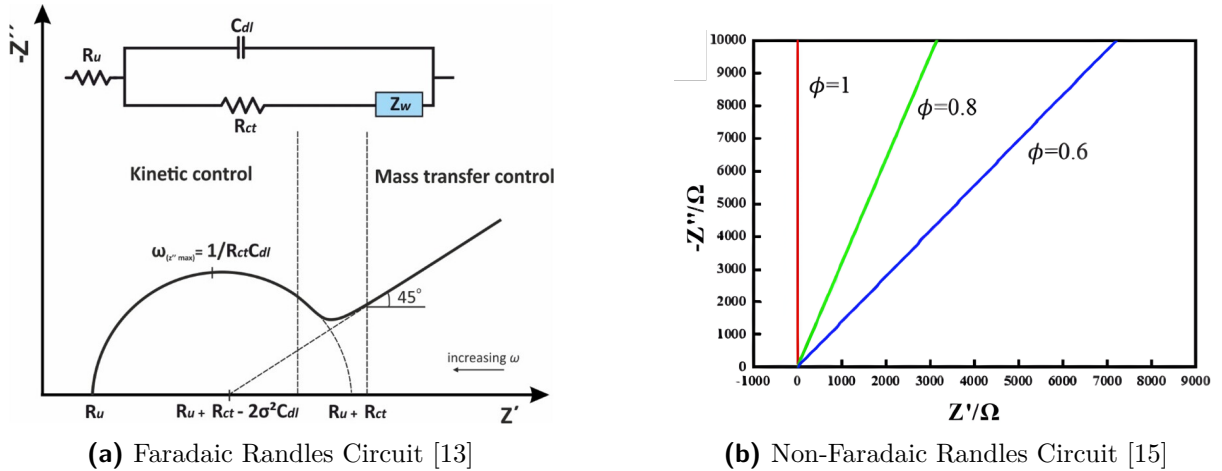
Figure 2.3: Nyquist Plots of Faradaic and Non-Faradaic Randles Circuits

The non-faradaic Randles equivalent, however does not exhibit a semi-circle, due to the exclusion of the charge transfer resistance (R_{CT}) and Warburg impedance (Z_w). Instead, the Nyquist plot appears as a straight line with an x-axis intercept representing R_S. For solid electrodes, however the line is not vertical as would be expected from the series combination of a resistive and purely capacitive element [15] (Figure 2.3b). The C_{DL} is thus replaced with a CPE in the circuit model to account for this non-ideal capacitive behaviour. The impedance of the CPE is given by equation 2.2, with ω representing the angular frequency, T being a constant related to capacitance, and α being an exponent between 0 and 1 that characterizes the deviation from ideal capacitive behaviour [15]. α

corresponds to the angle of the line in the Nyquist plot. When $\alpha = 1$, the CPE behaves as an ideal capacitor, while values less than 1 indicate increasing non-ideality due to factors such as surface roughness or inhomogeneities [15].

$$Z_{CPE} = \frac{1}{T(j\omega)^\alpha} \tag{2.2}$$

2.3.2. Bode Plots

A Bode plot presents the magnitude, $|Z|$, and phase, ϕ, of the impedance as functions of frequency on a logarithmic scale. The Bode magnitude plot reveals how impedance changes with frequency, while the phase plot shows the transition between resistive ($\phi = 0°$) and capacitive ($\phi = -90°$) behaviour. While Nyquist plots offer direct visualization of resistive and capacitive interactions, Bode plots highlight the frequency dependence and allow clearer distinction of time constants [16]. In EIS analysis, both representations are complementary: Nyquist plots assist model-based fitting, whereas Bode plots verify consistency and highlight transition frequencies.

2.4. Impedance Analysers

Impedance analysers integrate signal generation, voltage and current measurement, and data processing to determine the complex impedance of a DUT. In biosensing, these devices perform EIS by applying a known AC excitation and measuring the resulting voltage and current responses over a range of frequencies. The ratio of these phasor quantities provides the frequency-dependent impedance, revealing biochemical interactions at the electrode–electrolyte interface.

Commercial solutions such as the PalmSens4, Gamry Reference 600+, and Metrohm Autolab PGSTAT offer exceptional accuracy, broad frequency ranges (typically 10 Hz to 1 MHz or higher), and advanced analytics including integrated equivalent circuit fitting. However, these instruments are prohibitively expensive ($\approx$ €4200 for the PalmSens4) and require significant technical expertise to interpret results. This makes them unsuitable for low-resource point-of-care settings where portability, cost, and ease of use are crucial. Miniaturised, low-cost impedance analysers are therefore being actively developed for POC applications [17–19]. Such designs prioritise simplicity, automation, and affordability, while maintaining sufficient frequency range and measurement accuracy to detect biological binding events.

2.4.1. Signal Generation

EIS requires the generation of a small AC excitation signal, either voltage or current, to probe the DUT. Generating or measuring voltage is simple as most modern electronics are voltage mode rather than current mode. On the other hand, generating a small current signal is difficult to do accurately and requires circuits such as the improved Howland current pump [20]. While measuring a current signal also has some complexity, it is significantly easier than generation and thus the method commonly used in EIS systems.

Voltage-based signal generation can use dedicated chips like the AD5933 or custom solutions using microcontroller-based digital-to-analogue converters (DACs). The AD5933 offers integrated frequency sweeps and impedance measurement, making it attractive for simple implementations. However, it has several critical drawbacks. The chip has a DC offset, which is problematic because biosensing requires bipolar signals with no DC component. DC bias causes charge accumulation at the electrode–electrolyte interface, establishing a net electrochemical potential that drives unwanted redox reactions. Over time, these parasitic reactions alter the interfacial chemistry and change the electrode's impedance characteristics, obscuring the dielectric and charge transfer properties that EIS aims to measure. The AD5933 also lacks direct voltage measurement capability and has a minimum measurable impedance of 1 kΩ, further limiting its suitability for biosensing applications.

In contrast, a DAC and analogue-to-digital converter (ADC) solution implemented on a microcontroller allows precise control of excitation signals, flexible signal processing, and easier integration with multiplexing and user interface subsystems. Direct measurement of the voltage across the DUT accounts for all sources of non-ideal behaviour—parasitic resistances, stray capacitance, drift, and environmental changes—providing accurate data for impedance calculation. This is vital in low-voltage biosensing where small changes significantly affect calculated impedance.

When generating sinusoidal signals using a DAC, the output is not a smooth analogue waveform but rather a series of discrete voltage steps. These steps introduce high-frequency components and harmonics not present in the original signal. Without filtering, they may interfere with downstream circuitry or cause aliasing during analog-to-digital conversion. An anti-aliasing filter (AA filter), typically a low-pass filter (LPF), is placed after the DAC output to remove high-frequency content and smooth the signal.

The dynamic range of a DAC, expressed in decibels, determines the smallest signal it can produce above its noise floor and is given by [21]:

$$\text{Dynamic Range} = 6.02n + 1.76 \tag{2.3}$$

where n is the number of bits of resolution. The AA filter must attenuate high-frequency components sufficiently so that aliased content falls below this noise floor, whilst main-

taining a flat passband response to avoid distorting the intended output's amplitude or phase.

For systems generating signals across wide frequency ranges, a fixed-frequency AA filter becomes unsuitable. A single cutoff frequency cannot accommodate both low and high signal frequencies without either excessive attenuation or inadequate filtering. Variable AA filters address this by allowing dynamic cutoff adjustment. Many require changing resistor values to set the cutoff frequency, which is impractical for rapid frequency changes. Clock-tunable filters, which adjust their cutoff based on an external clock signal, offer a more flexible solution for wide frequency sweeps.

2.4.2. Voltage Measurement

Accurate voltage measurement across the DUT is essential for impedance calculation. Some designs infer voltage by using the known characteristics of the applied signal [17], but this fails to account for parasitic resistances, stray capacitance, drift, and environmental changes. Direct measurement captures all these variations, leading to reliable impedance calculations, particularly in low-voltage biosensing where errors significantly impact results. The voltage must be measured directly across the biosensor itself, rather than only relative to a fixed reference, to ensure that dynamic behaviours at the sensor-electrolyte interface are accurately reflected.

Two common circuits for differential voltage measurements are differential op-amps and instrumentation amplifiers. Differential op-amps are simple and cost-effective but are susceptible to common-mode noise and offset errors [22]. They also have relatively low input impedance, which loads the signal source and affects measurements [22]. Instrumentation amplifiers are specifically designed for high-precision differential measurement. They provide superior common-mode rejection, high input impedance, and excellent accuracy even with small signals in noisy environments [23]. This makes them particularly suitable for biosensing where signals can be very small and minimising interference is critical.

Amplifying the measured voltage to fully utilise the ADC's linear range enhances both sensitivity and resolution. By maximising the voltage swing within the ADC's input range, the system can discriminate smaller changes in sensor response, allowing better detection of low-concentration analytes. However, amplification introduces trade-offs related to gain-bandwidth product, which limits usable bandwidth at higher gains. Multi-stage amplification distributes gain across several stages, allowing higher overall gain whilst maintaining adequate bandwidth across the measurement frequency range.

2.4.3. Current Measurement

Accurate current measurement is essential for determining the impedance of the DUT. Two primary approaches exist, namely shunt resistor-based measurement and transimpedance

amplifier-based measurement.

The most basic method places a small, known precision resistor (shunt resistor) in series with the current path and measures the voltage drop across it. Ohm's Law then gives the current. This approach is cheap and easy to implement but has severe drawbacks. The voltage drop across the resistor directly reduces the magnitude of the applied perturbation to the DUT, impacting measurements. For biosensing, where signal levels are already low, even small drops significantly affect sensitivity.

A transimpedance amplifier (TIA) converts input current to proportional output voltage without introducing significant voltage drop across the DUT. The TIA makes use of the following properties of op-amps:

$$V_n \approx V_p \tag{2.4}$$

$$I_n \approx I_p \approx 0 \tag{2.5}$$

where V_n and V_p are the voltages at the inverting and non-inverting inputs respectively, and I_n and I_p are the input bias currents. The positive input (connected to the DUT) is driven to the same potential as the negative input (ground or reference voltage), thereby ensuring a low-impedance path for the current. Conversely, equation 2.5 ensures that the TIA has a high input-impedance and that the current from the sensor flows entirely through the feedback resistor. The output voltage is then given by:

$$V_{out} = I_{in} \times R_{feedback} \tag{2.6}$$

The TIA has the advantage that unlike a shunt resistor, the feedback resistor can be large without affecting the applied signal.

In biosensing with fixed voltage perturbation, current varies dramatically depending on the DUT's impedance; from nanoamperes at high impedance (low analyte concentration) to milliamperes at low impedance (high analyte concentration). A fixed-gain amplifier is impractical across this dynamic range. It would either saturate at high currents or provide insufficient resolution at low currents. Variable gain amplification, achieved through switchable feedback resistors in the TIA or programmable gain amplifiers (PGAs) in subsequent stages, allows the system to adapt to current magnitude. This ensures output voltage remains within the optimal range for the ADC whilst maximising measurement resolution.

2.5. Related Works

Chapter 3

Design

3.1. Design Philosophy

The aim of this project is to design a impedance spectroscopy system that can be used in a point-of-care setting. Tim Brown's design thinking principles [24] are thus well suited and were used as the bases for the design process. Brown's approach is characterised by five stages: empathising with the end user, defining a clear problem statement, ideating a wide range of creative ideas, building a quick prototype, and finally testing. These phases are cyclical and allow rapid iteration and learning. This project represents the culmination of this design process, although further iterations of the design process could allow further refinement of the end product.

3.1.1. Understanding the end user

Point-of-care (POC) diagnostic devices are essential for decentralized healthcare, particularly in resource-limited settings such as rural clinics and community health facilities. While EIS has proven to be a powerful technique for biosensing applications, existing solutions present significant barriers to widespread adoption in POC environments.

Commercial impedance analysers such as the PalmSens4 offer exceptional technical capabilities, including frequency ranges from $10\,\mu$Hz to 1 MHz, high resolution (18-bit), and data analysis features such as circuit modelling [25]. However, these instruments have two critical limitations for POC applications. Firstly, they require substantial technical expertise to interpret EIS data, as users must understand the underlying electrochemical principles to extract meaningful diagnostic information. Secondly, commercial systems like the PalmSens4 are prohibitively expensive, with prices €15,000, making them impractical for widespread deployment in clinics, rural health centres, or low-resource settings.

Previous academic projects have successfully demonstrated low cost impedance spectroscopy devices [26] [18] [17], but similarly require users to manually analyse impedance spectra and possess an understanding of EIS principles to interpret the results. This technical barrier prevents POC personnel from using these devices effectively.

POC healthcare providers require a device that performs impedance-based biosensing but abstracts the complexity away from the user, presenting results in an intuitive way.

Quantitative results, rather than qualitative results are sufficient to indicate the need for referral to a specialist and further testing.

3.1.2. Problem Statement

How can we design a low-cost, easy-to-use impedance analyzer for biosensing applications that eliminates the need for specialized knowledge, enabling point-of-care personnel to test for multiple biomarkers?

This problem statement encapsulates three critical design requirements :

1. Accessibility: The device must process raw impedance measurements and convert them to meaningful outputs, removing the need for users to understand Nyquist plots, equivalent circuit models, or phase angle analysis. Running from a battery and being able to operate without a computer are also necessities in rural settings.

2. Affordability: The total system cost must remain under R4,500 (approximately €220), making it orders of magnitude more affordable than commercial alternatives like the PalmSens4 at €15,000, thereby enabling widespread deployment in resource-limited settings.

3. Multiplexing capability: In resource constrained POC environments, healthcare professionals often face high patient loads. Due to this, multiplexed POC testing is of increasing importance for clinical screening [27]. This allows the screening of multiple analytes with minimal involvement from healthcare professionals.

3.2. Functional Design Overview

The system can be broken up into multiple subsystems, each fulfilling a specific function in order to create a complete device that meets the requirements. On the most basic level the device consists of the DUTs, an impedance analyser and a user interface. The DUT is the biosensor that interacts with the analyte and whose impedance characteristics change based on the analyte concentration. A multiplexer is used to interface between multiple DUT's and the impedance analyser. The impedance analyser can be further broken down into the power electronics, excitation stage, voltage and current measurement stages and finally the processing that uses an STM32. The user interface is based on an ESP32 and communicates with the impedance analyser through UART.

Breek impedance analyser op in further subsystems Discuss wat ons wil bereik en hoe ons dit gan opbreek. Beskryf hoe die circuit die beginsels van biosensors en EIS in ag moet neem, basies wat dit moet doen, hoekom multiplexing en ja dan hoe daai overall doel in gedeeltes opgebreek word.
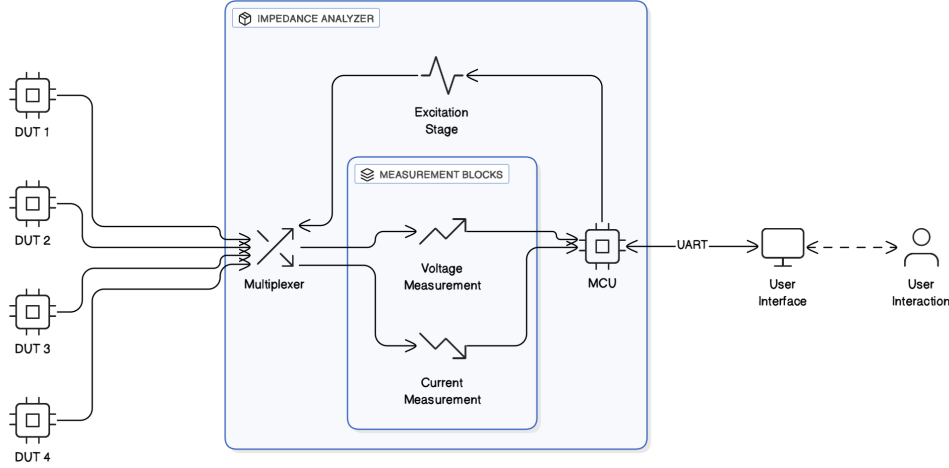
Figure 3.1: System Overview

3.3. Analogue Frontend Design

3.3.1. Excitation

The easiest way of producing a controlled voltage signal is using a DAC. Both dedicated DACs and DACs built into microcontroller units (MCUs) were possible options.

To avoid establishing a DC bias at the electrode–electrolyte interface, the generated excitation must be centred around a stable reference potential. This can be achieved by shifting the DAC output to be biased around ground using a level-shifting op-amp circuit. However, this requires providing all analogue circuitry with a negative supply rail. This project instead uses a buffered virtual ground reference at 1.65 V (3.3 V/2) as the midpoint for all analogue circuitry. This approach ensures no DC bias is applied to the DUT whilst negating the need for negative supply rails.

The anti-aliasing filter must provide sufficient attenuation at the Nyquist frequency ($f_s/2$) to ensure any aliased content falls below the DAC's noise floor. For the 12-bit DAC found in the STM32F303K8, equation 3.1 gives a dynamic range of 74 dB.

$$\text{Dynamic Range} = 6.02n + 1.76 \tag{3.1}$$

The filter's passband must remain flat at the desired signal bandwidth to avoid distorting the amplitude or phase of the intended output. Due to these requirements, a fixed frequency AA filter is unsuitable when generating frequencies from 1 Hz to 100 kHz. Many variable AA filter ICs exist, but most require changing resistor values to set the cutoff frequency, which is impractical when many frequencies are needed.

The LTC1069 proved to be the only viable option. It provides an 8th order lowpass filter that approximates a raised cosine response (with $\alpha = 1$). It has a cutoff frequency of up to 120 kHz (200 kHz when using ±5 V supply rails) set by an external clock and a
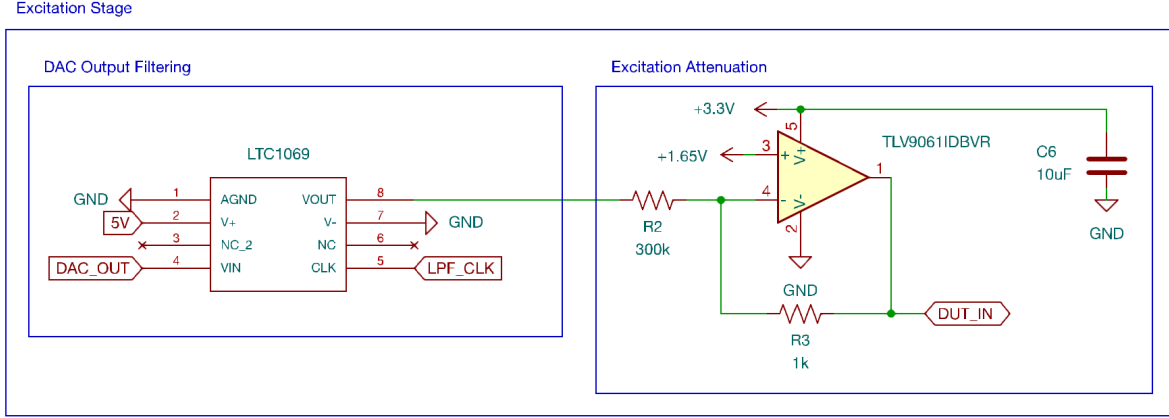
Figure 3.2: Complete Excitation Stage Circuit

linear phase response [28]. The clock-tunable nature is ideal for this project, allowing easy adjustments through a timer on the STM.

To maximise voltage resolution and minimise noise, the full linear range of the DAC is utilised when generating the signal. This requires that the DAC output signal is attenuated from 3 Vpp to the desired 10 mVpp using an inverting op-amp. From equation 3.2, $R_f = 1k\Omega$ and $R_{in} = 300k\Omega$ can be calculated as suitable values.

$$A_v = \frac{V_{out}}{V_{in}} = -\frac{R_f}{R_{in}} \tag{3.2}$$

3.3.2. Voltage Measurement

The voltage measurement stage is responsible for accurately measuring the voltage across the DUT during excitation. The expected voltage levels across the DUT are in the range of 10 mVpp, which is too small to be measured directly by the ADC of the STM32F303K8, which has an input range of 0-3.3 V. To fully utilise the ADC's resolution and sensitivity, the voltage signal must be amplified to match the ADC's input range. This requires a gain of approximately 300 V/V (from 10 mVpp to 3 Vpp). However, amplifying the signal by such a large factor in a single stage would introduce significant phase shifts and gain reductions at higher frequencies due to the gain-bandwidth product limitations of op-amps. To mitigate this, a two-stage amplification approach is employed.

The INA331 instrumentation amplifier was selected for the first stage of voltage measurement due to its combination of low offset voltage, high common-mode rejection and low input bias current. The INA331 features a typical offset voltage of 250 µV, which represents the inherent DC error between the input terminals when no differential signal is applied. It directly adds to the measured voltage, creating a systematic DC error that must be considered in calibration. The low input bias current of 0.5 pA avoids loading the DUT and influencing current measurements.

The device provides an internal gain of 5 V/V, configurable to higher gains through external resistors according to the relationship $G = 5 + 5 \times \frac{R_2}{R_1}$. Choosing $R_1 = 1k\Omega$ and $R_2 = 2k\Omega$ results in a gain of 15 V/V.

Discuss why bandwidth is important instead of jumping straight into it Gain-bandwidth product (GBW) represents the -3 dB bandwidth of an op-amp at unity gain. The -3 dB bandwidth of the op-amp can be calculated for a specific gain using equation 3.3, where A_{noise} represents the noise gain calculated in equation 3.4. The use of noise gain accounts for non-ideal feedback effects and circuit imperfections [29].

$$f_c = \frac{GBW}{A_{noise}} \tag{3.3}$$

$$A_{noise} = 1 + \frac{R_f}{R_{in}} \tag{3.4}$$

The gain and phase shift at any frequency can be calculated based on the cutoff frequency using equations 3.5 and 3.6 respectively [30], with $\omega = 2\pi f$ and $\omega_0 = 2\pi f_c$.

$$|H(j\omega)|_{dB} = 20 \log \frac{1}{\sqrt{1 + \frac{\omega^2}{w_0^2}}} \tag{3.5}$$

$$\varphi(\omega) = -\tan^{-1}(\frac{\omega}{\omega_0}) \tag{3.6}$$

Equations 3.3 and 3.4 are not applicable to instrumentation amplifiers due to their three op-amp design. However, the bandwidth can be estimated from the datasheet to be 2.3 MHz (as seen in figure 3.3) at the chosen gain. Using equations 3.5 and 3.6, the gain reduction and phase shift at 100 kHz can be estimated as -0.004 dB and -2.49° respectively. While this still needs to be accounted for during calibration, it represents a very flat and linear response leading to a more accurate system.
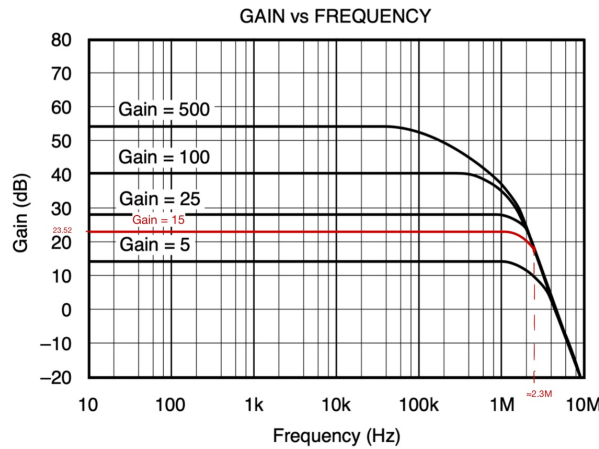

Figure 3.3: INA331 Bandwidth vs Gain adapted from [**?**]

The second stage uses a TLV9061 op-amp in an inverting gain configuration. With a

GBW of 10 MHz and gain of $A_v = -20$ ($A_{noise} = 21$), the expected bandwidth is 476.2 kHz (equation 3.3). From equations 3.5 and 3.6, an expected -0.094 dB gain reduction and -11.86° phase shift is calculated at 100 kHz. However, this does not need to be calibrated for as an identical gain stage will be used for the current measurement, ensuring that any gain reductions and phase shifts are cancelled out during impedance calculation.

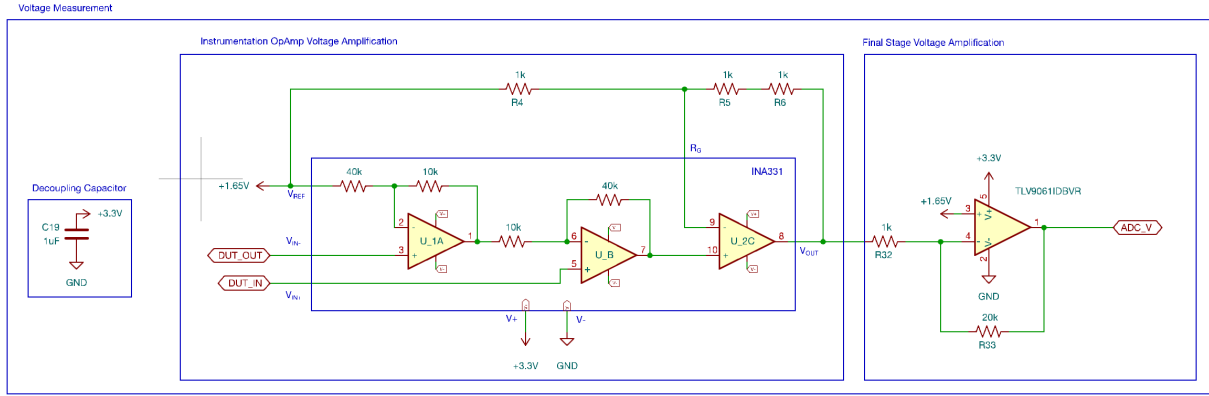The final circuit for voltage measurement can be seen in figure 3.4.

Figure 3.4: Complete Voltage Measurement Stage Circuit

3.3.3. Current Measurement

The current measurement stage represents the most complex and arguably most important aspect of the analogue frontend. Accurate current measurement across a wide dynamic range is essential for reliable impedance determination.

The architecture consists of three stages: a TIA provides the initial current-to-voltage conversion, followed by a PGA, then a final inverting gain op-amp stage. This final stage is identical to the second voltage measurement stage, ensuring that gain reductions and phase shifts cancel during impedance calculation.

Based on measurements of the biosensor using the PalmSens4, the expected impedance ranges from $100\,\text{k}\Omega$ at 1 Hz to $10\,\Omega$ at 100 kHz. For a fixed 10 mVpp excitation, this corresponds to a current range from 100 nA to 1 mA, spanning four orders of magnitude. This wide dynamic range drives several critical design requirements.

A fixed-gain amplifier is impractical across this range. High gain would saturate at high currents, whilst low gain would not utilise the full ADC range at low currents. Programmable gain is therefore essential. This is achieved through two mechanisms: switchable feedback resistors in the TIA and variable gain in the PGA stage.

The PGA113 offers gains ranging from 1-200 V/V with a high GBW of 10 MHz and is controlled via SPI. It has a low gain error of $\leq 0.3\%$ and extremely low noise at 12 nV/$\sqrt{\text{Hz}}$. Combined with the final TLV9061 gain stage (identical to the final voltage measurement stage), this provides variable gain from 20-4000 V/V after the TIA. The STM32F303K8 also has an internal PGA with an 8 MHz GBW and binary gains from 2^1 to 2^4, however

Figure 3.5: Example of Kelvin Sense Switch Connections and High Impedance Buffer [1]

it was unclear whether the added flexibility of a second PGA would outweigh the added noise of an additional gain stage. The PCB was thus designed with a jumper allowing the internal PGA to be bypassed. After testing, it was decided that the STM's PGA would not be used.

While the TIA's feedback resistor can be large without affecting the applied signal to the DUT, it reduces the bandwidth. If $R_{feedback}$ is too large, the TIA experiences significant phase shifts and reduced gain at higher frequencies (referring back to equation 3.3). Using multiple gain stages distributes the amplification, allowing the TIA to use a moderate feedback resistor whilst maintaining adequate bandwidth.

Multiple feedback resistor paths on the TIA itself provide additional benefits beyond bandwidth. They enable finer gain segmentation across the input current range, improving measurement precision. The larger feedback resistor handles low currents with maximum resolution, whilst the smaller resistor prevents saturation at high currents. This ensures smooth transitions between gain settings without gaps where currents would be too large for one resistor but too small for the other.

The OPA3S328 is specifically designed for TIA applications, with a wide GBW of 40 MHz, 0.2 pA input bias and typical input voltage offset of $10\,\mu$V. Importantly, it has integrated switches for switching between feedback resistors. However, the switch on-resistance is non-negligible at 90–125 Ω and varies with temperature. This produces gain errors and distortion on the TIA output. This can be addressed by using the second switch and op-amp integrated into the OPA3S328 package to build a buffered multiplexer. An example of this circuit is shown in Figure 3.5. The switch senses the TIA output directly at the feedback resistor for each gain, whilst the second op-amp acts as a buffer. The low input bias current of the op-amp ensures negligible voltage drop (a worst case of 1.25 nV), providing an accurate Kelvin sense connection. This eliminates gain error, gain error drift and gain non-linearity due to the switch resistances.

The YBJ variant was chosen due to its 3-way multiplexer (MUX) over the RGR variant with a 2-way MUX, enabling finer gain segmentation and improved measurement precision across the input current range. However, due to the small package size and PCB manufacturing limits (see section 3.5), only two of the three switches were used.

To maximise the ADC's range even at the smallest current, the larger feedback resistor is designed to deliver 3 Vpp at the maximum PGA gain. From equations 3.7–3.9, this results in 7.5 kΩ.

$$V_{TIA} = \frac{3}{4000} = 750\mu V \tag{3.7}$$

$$A_{TIA} = \frac{750\mu V}{100nA} = 7500V/A \tag{3.8}$$

$$\therefore R_{f1} = 7.5k\Omega \tag{3.9}$$

The smaller feedback resistor is chosen to give the same overall gain at the maximum PGA gain as the larger resistor gives at the minimum PGA gain. This ensures a smooth transition between feedback resistors with no currents being too large for the larger feedback resistor but too small for the smaller one. The smaller feedback resistor is calculated to be 200 times smaller at $R_{f2} = 37.5\Omega$. This ensures that the ranges from 50 nA - 20 μA and 20 μA - 4 mA are covered respectively, whilst ensuring that the ADC input stays between 1.5 - 3 Vpp.

In traditional TIA designs a capacitor is placed in parallel with the feedback resistor to provide sufficient phase margin and ensure stability [2]. These designs are, however, intended for use with a photodiode, rather than EIS. There are few sources available that discuss the design of a TIA for EIS purposes, where capacitance is what is measured rather than compensated for. These sources do not discuss the necessity of feedback capacitors, thus this has to be derived from theory.

The dominant pole of the open loop response of an op-amp is a function of the GBW and the open loop gain, A_{OL} (equation 3.10). This determines the -3dB frequency of the open loop transfer function and after this point the gain rolls of at a rate of -20dB/decade. Due to the extremely large open loop gains of modern op-amps (130dB or $3.16 \times 10^6 V/V$ for the OPA3S328), negative feedback is required between the output and inverting input. The amount of the output that is fed back to the input is defined as the feedback factor (β) and described by equation 3.11. Where V_{fb} is the voltage present at the inverting input of the op-amp and V_{out} the voltage at the output. This negative feedback results in the closed loop gain (equation 3.12) where the loop-gain refers to $A_{OL} \times \beta$ (equation 3.13).

$$\text{Dominant Pole} = f_{DP} = \frac{\text{GBW}}{A_{OL}} \tag{3.10}$$

$$\text{Feedback Factor} = \beta = \frac{V_{fb}}{V_{out}} \tag{3.11}$$

$$\text{Closed Loop Gain} = A_{CL} = \frac{A_{OL}}{1 + A_{OL}\beta} \tag{3.12}$$

$$\text{Loop Gain} = A_{OL}\beta \tag{3.13}$$

$$\tag{3.14}$$

When the loop-gain is -1, equation 3.12 simplifies to $A_{CL} = \frac{A_{OL}}{0}$ and the system becomes unstable. This happens when V_{fb} leads or lags V_{out} by 180°. The phase margin (PM) is thus defined as in equation 3.15 and describes how close the system is to a 180° phase shift and instability when the loop gain is at 0dB or 1V/V (the critical point or f_c). From equation 3.17 it is shown that this happens when the magnitude plots of A_{OL} and $\frac{1}{\beta}$ intersect. To ensure stability, the PM should be at least 45°, with higher values providing more stability at the cost of transient response [2]. The phase margin can be calculated by subtracting the phase of $\frac{1}{\beta(j\omega)}$ from the phase of $A_{OL}(j\omega)$ to get the phase of $A_{OL}\beta(j\omega)$.

$$\text{PM} = 180° + \varphi_{A_{OL}\beta} \text{ at } |A_{OL}\beta| = 0dB \tag{3.15}$$

$$|A_{OL}\beta| = 0dB = 1V/V \tag{3.16}$$

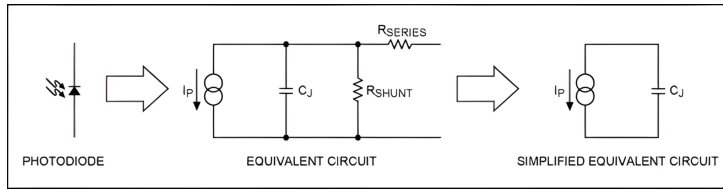$$\therefore |A_{OL}| = |\frac{1}{\beta}| \text{ at } f_c \tag{3.17}$$

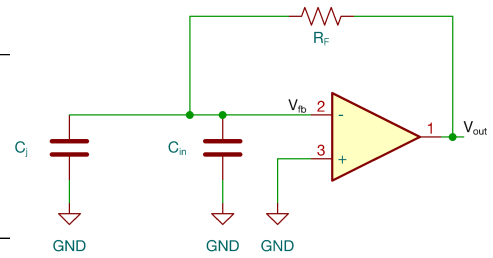**Figure 3.6:** Photodiode equivalent circuit [2]

Figure 3.7: Equivalent TIA circuit for photodiodes

$$C_i = C_j + C_{in} \tag{3.18}$$

$$\beta(j\omega) = \frac{X_{c_i}}{R_f + X_{C_i}} = \frac{1}{1 + j\omega R_f C_i} \tag{3.19}$$

$$\therefore \frac{1}{\beta(j\omega)} = 1 + j\omega R_f C_i \tag{3.20}$$

Figure 3.6 shows the simplified equivalent circuit of a photodiode, including the junction capacitance (C_J). With figure 3.7 showing the resulting equivalent circuit model of a TIA for measuring photodiodes, including the input capacitance of the op-amp (C_{in}). From this, the feedback factor can be calculated as seen in equation 3.19. The pole in $\beta(j\omega)$, caused by the combined input capacitance, translates to a zero in $\frac{1}{\beta(j\omega)}$. This zero causes the magnitude of $\frac{1}{\beta(j\omega)}$ to increase at a rate of 20dB/decade after the corner frequency (determined by the value of C_i) and the phase to increase from 0°to 90°. The result is a very small phase margin at the critical frequency and instability (as seen in figure 3.11). The feedback capacitor in parallel with R_f solves this by adding a pole to $\frac{1}{\beta(j\omega)}$, cancelling out the zero and thus adding phase margin.
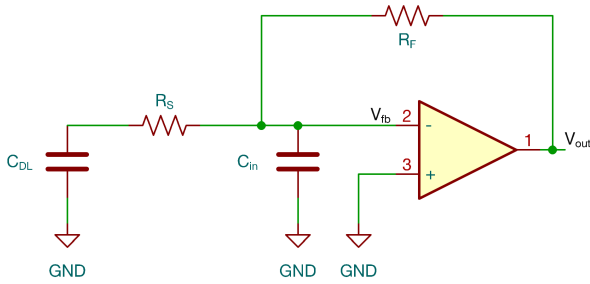

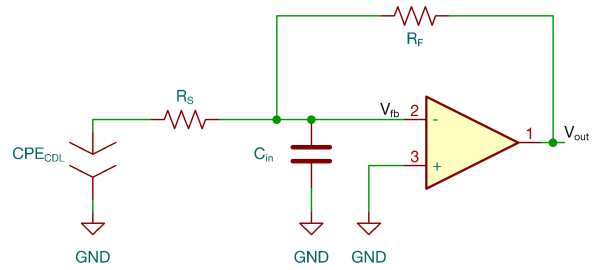**Figure 3.8:** Simplified Randles equivalent TIA circuit with ideal capacitance

Figure 3.9: Randles equivalent TIA circuit with CPE

Simplified Randles Circuit with Ideal Capacitance:

$$Z_{in} = (R_S + X_{C_{DL}})||X_{C_{in}} \tag{3.21}$$

$$\beta(j\omega) = \frac{Z_{in}}{R_f + Z_{in}} \tag{3.22}$$

$$\therefore \frac{1}{\beta(j\omega)} = 1 + \frac{R_f}{Z_{in}}$$

$$= 1 + \frac{R_f}{(R_S + X_{C_{DL}})||X_{C_{in}}} \tag{3.23}$$

Full Randles Circuit with CPE:

$$Z_{CPE} = \frac{1}{T(j\omega)^\alpha} \tag{3.24}$$

$$Z_{in} = (R_S + Z_{CPE})||X_{C_{in}} \tag{3.25}$$

$$\beta(j\omega) = \frac{Z_{in}}{R_f + Z_{in}} \tag{3.26}$$

$$\therefore \frac{1}{\beta(j\omega)} = 1 + \frac{R_f}{Z_{in}}$$

$$= 1 + \frac{R_f}{(R_S + Z_{CPE})||X_{C_{in}}} \tag{3.27}$$

However, the equivalent Randles circuit model of a biosensor differs fundamentally from the model of a photodiode due to the series resistance R_s. Figures 3.9 and 3.8 show the equivalent TIA circuits for a non-faradaic Randles circuit and a simplified model using an ideal capacitance (C_{dl}) instead of the CPE by approximating $T = C_{dl}$ and $\alpha = 1$. For the simplified model, the input impedance and feedback factor can be calculated as seen in equations 3.21 - 3.22. The full Randles non faradaic equivalent circuit results in 3.26. The series resistance and double layer capacitance of the biosensor was estimated using PS Trace and values for input capacitance, open loop gain and gain bandwidth were read from the OPA3S328 datasheet. A MatLab script was then used to calculate the $\frac{1}{\beta(j\omega)}$ transfer function and loop gain of the system. Similairly the series resistance, T and α values were estimated for the Randles circuit using circuit fitting in PS Trace and plotted in MatLab. The response of the equivalent photodiode model was also plotted using the constant C_{DL} as the parasitic junction capacitance. Table 3.1 shows the estimated circuit paramaters and figures 3.11 and 3.10 shows the resulting responses. Table 3.2 lists the calculated critical frequencies and phase margins.
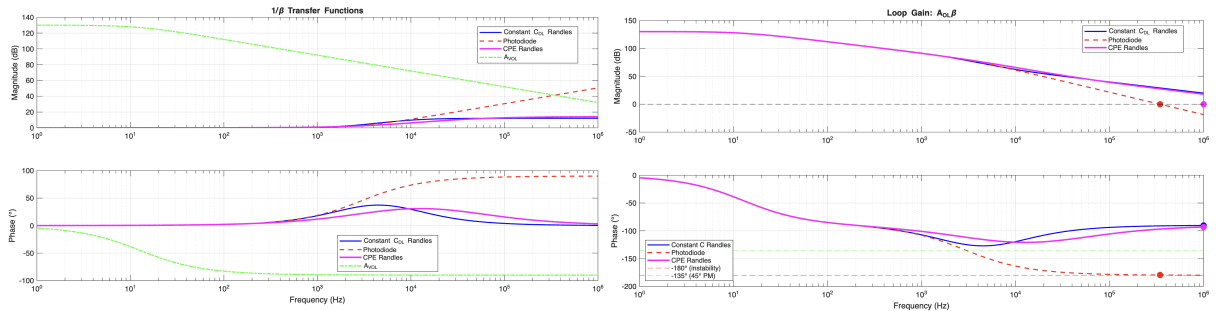
(a) $\frac{1}{\beta(j\omega)}$ frequency response

(b) Loop Gain frequency response

Figure 3.10: Calculated frequency responses for $R_F = 37.5\Omega$

(a) $\frac{1}{\beta(j\omega)}$ frequency response
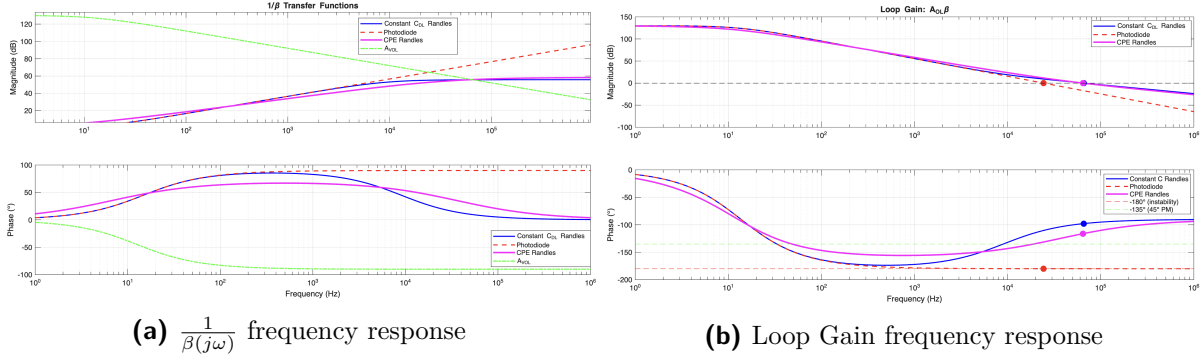
(b) Loop Gain frequency response

Figure 3.11: Calculated frequency responses for $R_F = 7.5k\Omega$

From these plots, the difference between the photodiode and biosensor circuits become clear. At low frequencies the simplified biosensor circuit closely follows the response of the photodiode. This is due to the zero caused by the capacitance dominating the response ($X_{C_{DL}} >> R_S$) and thus the equivalent circuits of the photodiode and Randles circuit are near identical. However, at higher frequencies R_S becomes much larger than $X_{C_{DL}}$ and the responses start to diverge. The dominance of R_S at higher frequencies ensure that ample phase margin is achieved by the critical frequency. The full Randles non-faradaic circuit model provides a more accurate representation of the biosensor TIA circuit and diverges earlier than the simplified circuit due to the CPE. This confirms that ample phase margin is available at both $R_f = 37.5\Omega$ and $R_f = 7.5k\Omega$, meaning that no feedback capacitors are needed. At extremely large values of R_F the phase margin reduces, and the system can become unstable ($R_f > 40k\Omega$ for this circuit). Since adding compensation capacitors reduces the bandwidth of the TIA [2], it is not recommended for biosensing TIA circuits, except in cases of extremely high feedback resistor values.

Table 3.1: Circuit Parameters

Parameter	Value
CPE Randles Circuit	
R_S	$8.975\,\Omega$
T	6.993×10^{-6}
α	0.785
C_{in}	$4.0\,\mathrm{pF}$
Constant C Randles Circuit	
R_S	$12.3\,\Omega$
C_{DL}	$1436.0\,\mathrm{nF}$
C_{in}	$4.0\,\mathrm{pF}$
Photodiode Equivalent	
C_i	$1436.0\,\mathrm{nF}$

Table 3.2: Stability Analysis Results

Configuration	f_c (kHz)	PM (°)	Status
$R_f = 7.5\,\mathrm{k\Omega}$			
Constant C Randles	65.83	82.2	Stable
Photodiode	24.22	0.1	Unstable
CPE Randles	64.22	63.8	Stable
$R_f = 37.5\,\Omega$			
Constant C Randles	9840.03	89.8	Stable
Photodiode	343.77	0.5	Unstable
CPE Randles	7725.81	86.3	Stable

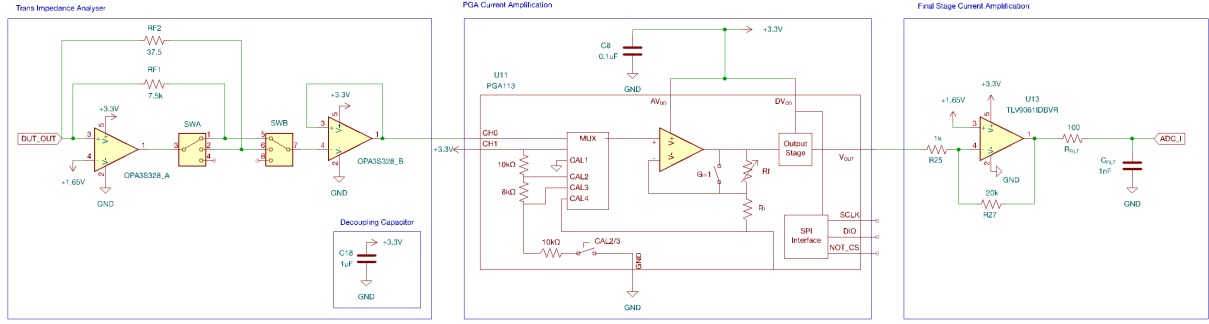The final current measurement circuit is shown in Figure 3.12.

Figure 3.12: Complete Current Measurement Stage Circuit

3.3.4. DUT

The design and manufacture of biosensors are outside the scope of this project. The biosensors described in [26] were used for this project, however the system could easily be adapted to work with other capacitive biosensors. To ensure ease-of-use, a method of interfacing with the biosensors that is simple and reliable needed to be developed. Spring-loaded battery connectors were used as they allow the DUT to be easily slid in and out of the device when combined with a 3d printed enclosure.

Insert 3d model of connectors, dut and 3d print.

3.3.5. Multiplexer

Two approaches towards multiplexing were considered. One approach is to have multiple excitation sources and measurement stages, allowing for simultaneous measurements of all DUTs. This approach has the advantage of speeding up the measurement process, while allowing each DUT to have electronics dedicated to its measurement range. The major disadvantages to this approach is complexity and cost.

Another approach is re-using the same excitation and measurement circuitry, by switching the input and outputs between the DUTs. This reduces the cost and complexity, but is reliant on having a reliable switching mechanism that does not impact the measurements.

Ultimately the best approach was using a single set of excitation and measurement circuitry, multiplexed in order to measure DUTs sequentially. The cost reductions of this approach outweighs the increased measurement time as no user input is required between DUT measurements.

Various options for multiplexers were considered including dedicated analogue multiplexers (MUX ICs), op-amp based multiplexers and relays. Dedicated analogue multiplexers consist of a collection of analogue switches. They typically use CMOS technology, resulting in compact integration and fast switching speeds. Modern analogue switches are available with very low on-resistance ($< 1\Omega$) and a high degree of flatness [31]. However, leakage

currents are inherent to these solid-state devices and can corrupt low-current signals, especially in the nanoampere range [31].

Op-amp-based multiplexers such as seen in Figure 3.13 provide buffering and impedance matching, which make them ideal for multiplexing voltage signals, but the buffering also make them unsuitable for use with current signals.
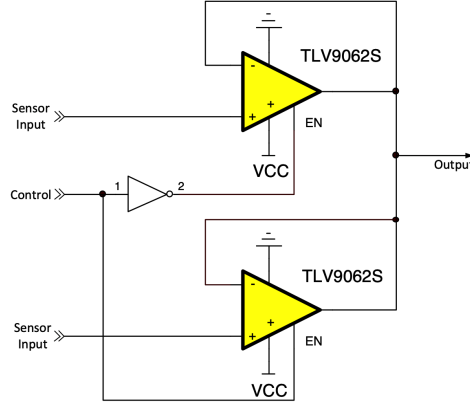

Figure 3.13: Op-amp based multiplexer circuit [3]

Signal relays, in contrast, use electromechanical contacts to physically open or close signal paths, offering near-zero leakage current and extremely low, stable contact resistance that is independent of signal voltage and temperature. This physical isolation and connection ensures that the measured current accurately reflects the biosensor response. While relays are slower to switch and larger than solid-state alternatives, their switching speed is more than sufficient for switching between sensors.

The TXS2-L2-3V DPDT latching signal relay was chosen due to its small size, low operating current (23.3 mA) and high mechanical lifetime (Minimum 200 000 operations). The major concern of a mechanical relay is the mechanical wear, however at an assumed 2 actuations per measurement and 50 measurements a day, the relays are expected to last more than 5 years. Utilising the DPDT topology of the relay, they can be configured in a tree pattern, allowing for 4 DUT's to be switched using 3 relays as seen in figure 3.14.

Despite the low operating current, a driver circuit is still needed to power the relay from a microcontroller GPIO. This consists of a lowside NPN transistor and a flyback diode to protect against voltage spikes when the coil is switched off. The final circuit can be seen in figure 3.15
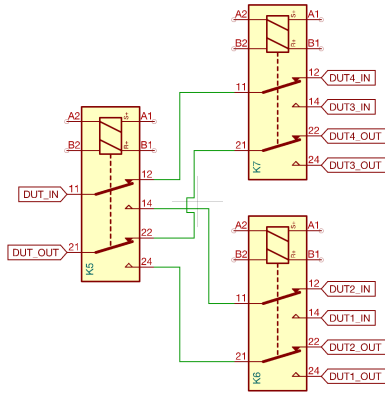
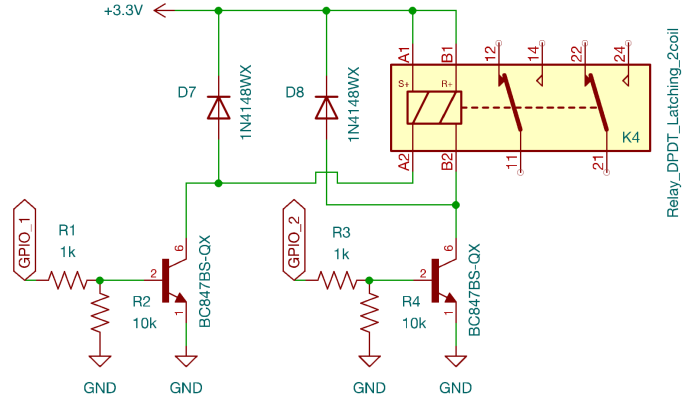**Figure 3.14:** Relay Multiplexer Topology for 4 DUT's

Figure 3.15: Relay Driver Circuit for one relay

3.3.6. Power Circuitry

With portability in mind, a battery is a requirement for the system. It was decided that the most cost-effective approach would be to utilise a microcontroller with built-in LiPo charging circuitry instead of a dedicated charging circuit as this is commonly available in many ESP32 boards. The 3.3V rail from the ESP will then be used to power the rest of the system.

As mentioned in Section 3.3.1, a 1.65V reference is needed for the analogue circuitry. Due to the small amplitude of the excitation signal, it needs to be highly accurate and stable. This was done through the use of a matched resistor array and a op-amp buffer. Using a resistor array ensures that our reference is the exact midpoint of the supply voltage despite any tolerances in the precise resistor value, while the op-amp buffers this output to avoid loading the resistor array and causing a voltage drop. Choosing a too large resistor value risks a slightly uneven voltage drop due to the input bias current of the op-amp buffer, on the other hand, a lower value increases the static current draw and power consumption. $1k\Omega$ was chosen as a balance between these tradeoffs.
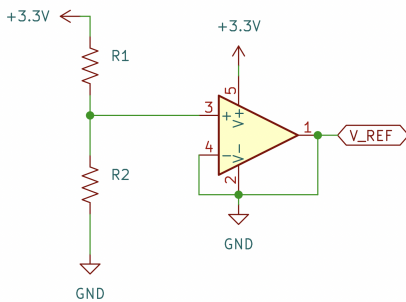

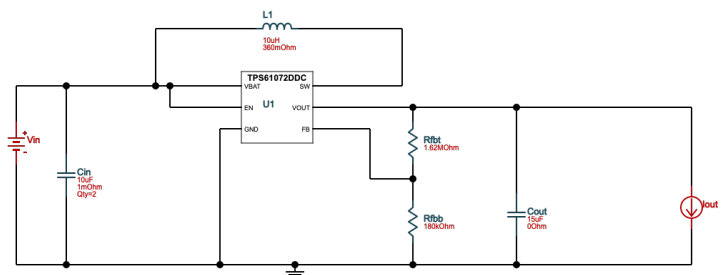
Figure 3.16: Virtual ground reference circuit

Figure 3.17: 5V boost converter circuit

The LTC1069 AA-Filter requires a 5V supply voltage. A 3.3V to 5V boost circuit was designed around the TPS61072 boost regulator using the TI WeBench power supply design tool [32], ensuring a stable and efficient circuit as seen in figure 3.17.

3.3.7. Signal Processing

3.3.8. User Interface

Fill in once GUI is actually done Talk about flexibility of having both physical buttons and display aswell as web ui, allowing both standalone use and use with either computer, tablet or cell phone, ensuring versatility across environments

3.4. Circuit Simulation

3.4.1. Biosensor

Despite the widespread use of CPEs in electrical simulations, the SPICE family of simulators lack a native CPE element. There are a variety of approaches to modelling CPEs such as Laplace transform, Fourier theory or using a network of resistors and capacitors. [33] builds on existing approaches to modelling a CPE using a combination of resistors and capacitors (such as Add references from wilson), by using an array of parallel RC elements as seen in Fig **??**. The branches form a theoretically infinite geometric progression of characteristic frequencies [33], however characteristic frequencies above and below the frequency range of interest are approximated using a single capacitor and resistor respectively. [33] provides MatLab code that calculates the R and C values of all the branches and this was used to model a CPE element matching the biosensor in LTSpice. Figure **??** shows that the CPE model does indeed exhibit a constant phase across the measurement range of interest (1Hz-100kHz) and figure **??** shows the simulated response of the biosensor including R_S. Comparing this to the PalmSens measurements (figure **??**) shows that this model serves as a fairly accurate representation of the DUT for simulation purposes.

3.4.2. Excitation stage

For the simulation of the excitation stage, a sample-and-hold block was used to mimic the DAC at varying sample rates. LTSpice has no included components to simulate a raised cosine filter, thus a FIR filter block from [34] with a raised cosine response and $\beta = 1$ was used. Comparing the simulated frequency response with the LTC1069-7 datasheet (Figures 3.18 and 3.19) for cutoff frequencies of 10kHz and 100kHz, the overall magnitude response is a good approximation, despite some differences at high levels of attenuation ($< -50dB$). The simulated phase response, however is non-linear which does not match

the LTC1069-7, but this will not impact the overall system simulation as the DUT is being excited at a single frequency. The TLV9061, INA331 and OPA3s328 PSpice models were obtained from TI and adapted to work in LT Spice. The TLV9061 was used for the attenuation stage.
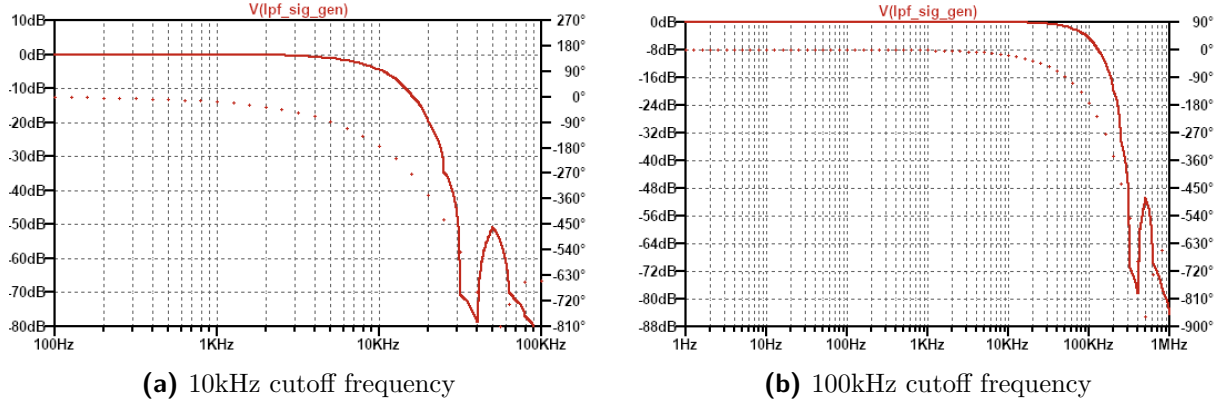

(a) 10kHz cutoff frequency

(b) 100kHz cutoff frequency

Figure 3.18: Simulated FIR filter frequency responses

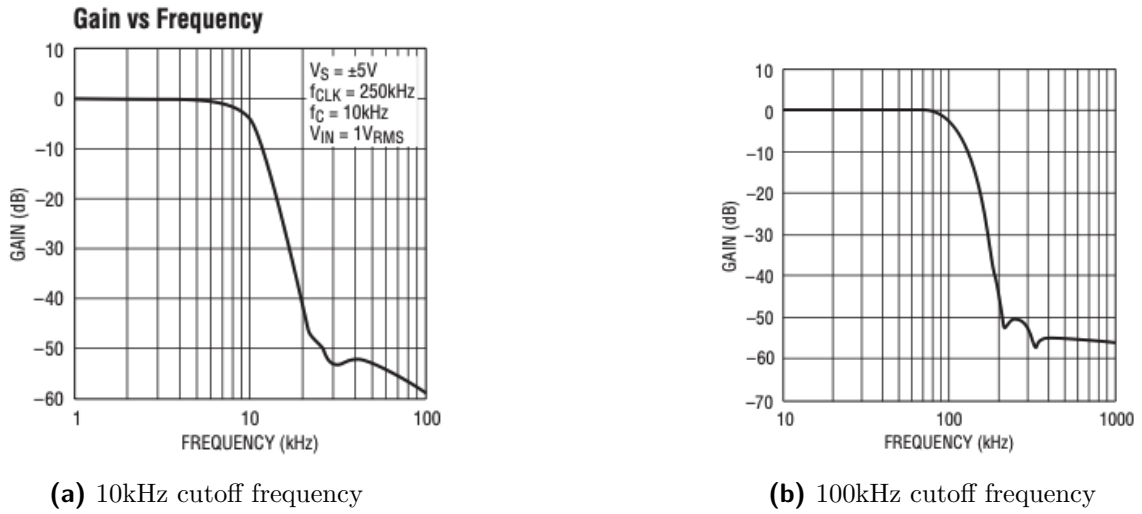**(a)** 10kHz cutoff frequency
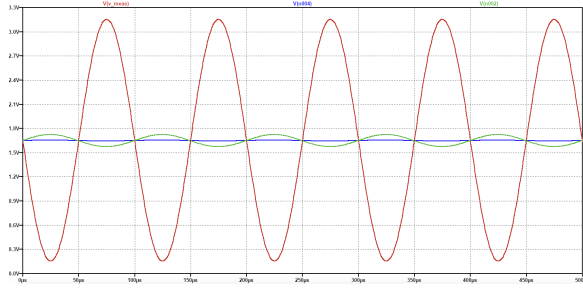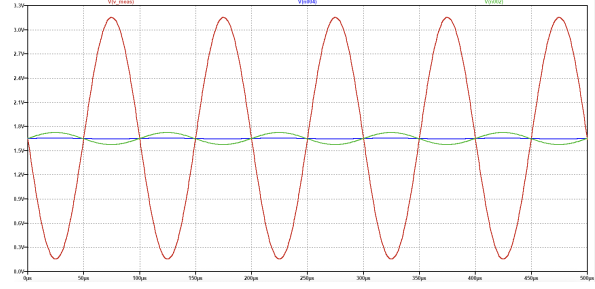
(b) 100kHz cutoff frequency

Figure 3.19: LTC1069-7 datasheet frequency responses

Figure 3.20a shows a 10kHz signal with 32x oversampling generated by the DAC before and after passing through the AA-filter and after being attenuated. Figure **??** shows current through the simulated DUT resulting from this signal.

(a) DAC output before and after AA-filter and attenuation

(b) Current through simulated DUT

Figure 3.20: Simulated excitation stage output and DUT response

3.4.3. Voltage measurement

The voltage measurement stage was simulated with the INA331 and TLV9061 models to confirm the frequency response of the system. Figure 3.21 shows only a slight gain reduction of -0.02dB gain reduction at 100kHz and a -4.6°phase shift. Fig 3.22 shows the overall frequency response of the voltage measurement stage with the TLV9061 amplification stage contributing an additional -0.2dB gain reduction and -3.4°phase shift. This confirms that sufficient bandwidth is available for measurements up to 100kHz.
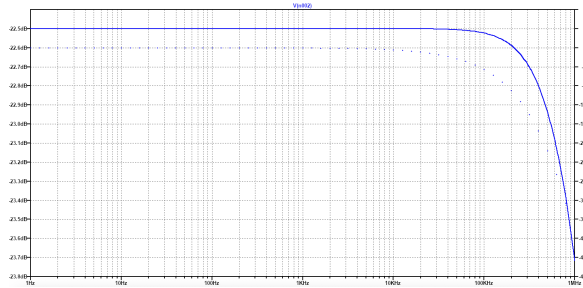
Figure 3.21: INA331 frequency response
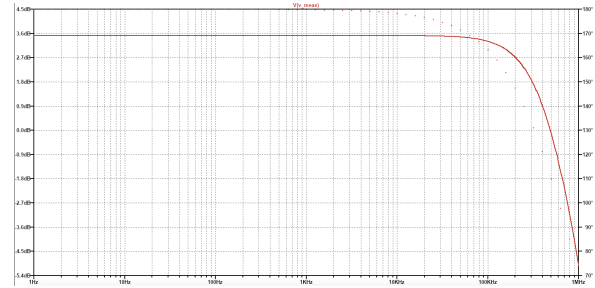
Figure 3.22: Complete voltage measurement stage frequency response

3.4.4. Current measurement

Due to problems porting the OPA3s328 PSpice model to LT Spice, the internal mux was not simulated. The PGA113 has no available PSpice model [35], thus a standard inverting amplifier configuration using the TLV9061 was used to simulate the PGA stage. Figure **??** shows the frequency response of the TIA stage alone at both feedback resistor values. At 100 kHz with $R_F = 7.5 \ k\Omega$, the stage exhibits a gain increase of +0.136 dB and a phase shift of -15.4°. For $R_F = 37.5 \ \Omega$, the response shows a gain increase of +0.137 dB and a phase shift of -15.6°. The slight gain increase is due to very slight peaking in the frequency response before the eventual rolloff. This demonstrates a very flat frequency response well below the circuit's bandwidth limitations. Figure **??** shows the overall frequency response of the current measurement stage with the PGA and final amplification stages contributing

an additional -0.25dB gain reduction and -4.8°phase shift. This confirms that sufficient bandwidth is available for measurements up to 100kHz.

To confirm the stability of the TIA circuit, Tian's method was used to plot the loop gain and phase margin for both the Radnles circuit using the CPE and the simplified circuit using a constant capacitance as seen in figure **??** and Table **??**. These results closely match the MatLab results in section 3.3.3, confirming that the TIA design is stable without the need for feedback compensation.

3.4.5. Complete System

The individual subsystems were combined into a complete model including DAC and ADCs using sample-and-hold blocks. Transient analysis was done at a range of excitation frequencies. For frequency analysis the DAC and ADCs were excluded.

3.5. PCB Design

Beskryf filosofie en idees wat mee ingegaa het. Briefly discuss general PCB design principles wat design geguide het (Analogue ground plane etc). Beskryf beperkings van PCB manufactures wat inag geneem moes word (PCB size, layers, trace width via diamtre etc.). Noem briefly hoekom PCB in China eerder as Uni laat maak. Gaan deur design logic en discuss probleem met TIA. Include maybe final PCB diagram en langs dit foto van manufactured PCB.

All PCB design was done using KiCad due to its open-source nature and wide usage in industry. Due to the complexity of the circuit, JLC PCB was used for manufacturing rather than Stellenbosch University's in-house PCB manufacturing. There are substantial price differences between JLC's standard process and their more advanced processes (\$4 vs \$68). Table 3.3 lists the key limits of JLC's standard PCB process that had to be taken into account.

Another key consideration when designing the PCB was minimising noise and interference in the analogue circuitry. Given the limitations of a two-layer PCB, maintaining a continuous and low-impedance ground reference was a key priority, as a fully dedicated ground plane was not practical. To achieve this, both layers incorporated extensive ground copper pours connected through frequent stitching vias to minimise loop inductance and reduce electromagnetic interference (EMI) coupling between layers. A single unified ground network was chosen over separate analogue and digital grounds, as is modern best practice for low-current mixed-signal systems [36]. Instead, the analogue and digital sections were physically partitioned, with sensitive analogue components and signal routed away from high-speed digital traces. Fencing vias were deployed along region boundaries to confine high-frequency digital currents and provide additional shielding for low-level analogue

signals (Figure **??**).

Subsystems we're grouped together with jumpers connecting subsystems, allowing for easier debugging and testing. Care had to be taken in selecting the pin usage for both the STM32 and ESP32 as nearly all pins on both devices were used. The small package size of the OPA3S328 (24-pin DSBGA with 0.4 mm pitch) also posed challenges for routing. With a minimum pad diameter of 0.25 mm and 0.4 mm pitch, the clearance between pads is only 0.15 mm, meaning that traces could not be routed between pads. Usually this would be solved using via-in-pads, however, the minimum via hole diameter of 0.3 mm meant that this was not possible with JLC's low cost PCB manufacturing process. By only using 2 of the 3 internal switches, OUTSB3 could be used to route the common node of switch B to the non inverting input of the buffer op-amp (Figure 3.25). This reduced the number of gain settings to 2 as mentioned in section 3.3.3.

The complete PCB schematic is shown in Appendix **??** and the final PCB layout in Figure 3.24.

Table 3.3: JLC PCB Standard Manufacturing Process Limits

Parameter	Limit
Minimum Trace Width	0.1 mm (4 mil)
Minimum Trace Spacing	0.1 mm (4 mil)
Minimum Via Diameter	0.45 mm
Minimum Via Hole Diameter	0.3 mm
Minimum BGA Pad Diameter	0.25 mm
Maximum Board Size	100 mm × 100 mm
Number of Layers	2, 4, or 6 layers
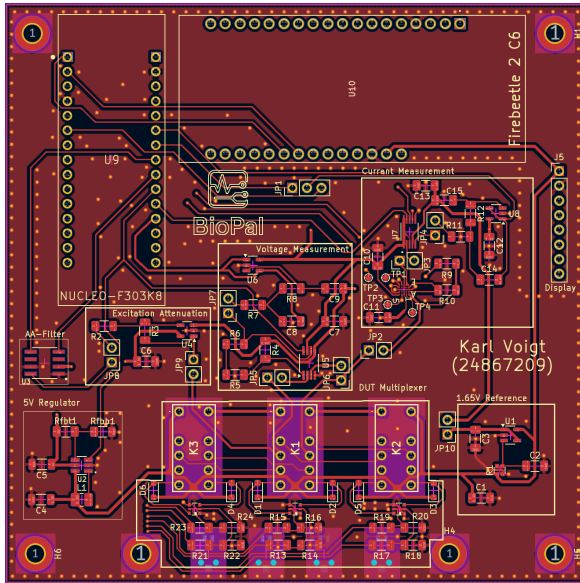
(a) PCB front layout
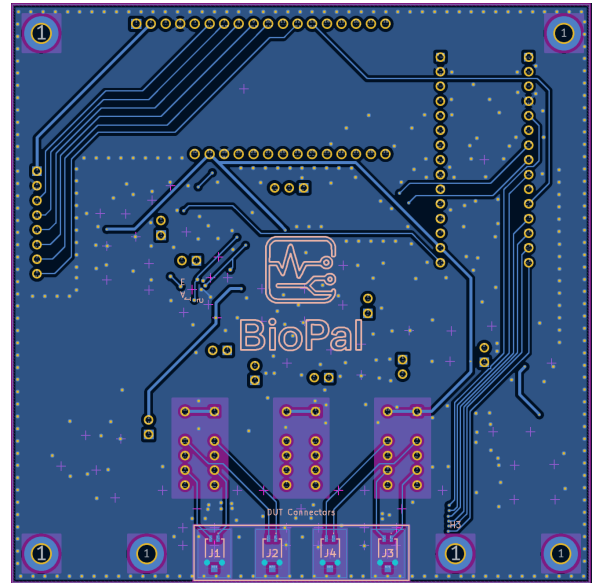
(b) PCB back layout

Figure 3.23: Final PCB layout

Figure 3.24: Final PCB render

Figure 3.25: OPA3S328 BGA routing solution

3.6. Firmware Development

The embedded system architecture was driven by the POC requirements of ease of use without technical expertise, versatility across diverse clinical settings and reliable measurements. To avoid dependence on external software and ensure the device can operate in any environment, all processing is performed on-device.
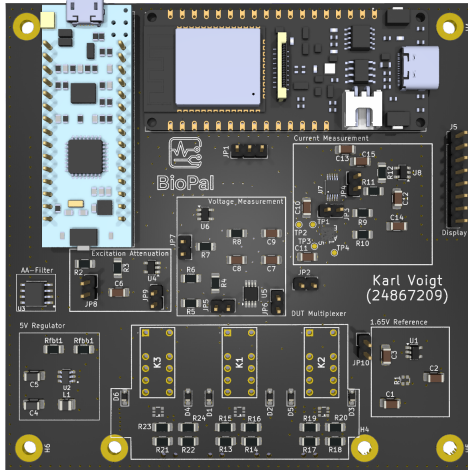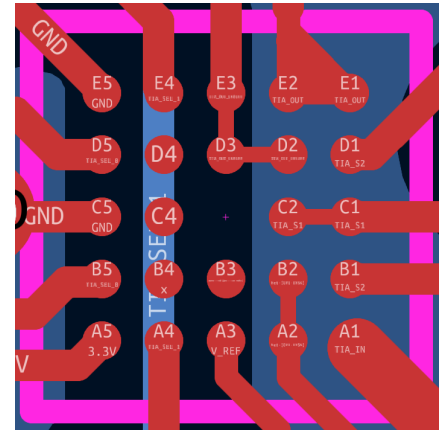
The system architecture is shown in Figure 3.26. The ESP32 C6 has ADC and DAC peripherals, but their performance is known to be suboptimal for high-precision measurement applications. Furthermore, the lack of direct timer control or direct memory access (DMA) support for these peripherals limits their usability for synchronous signal generation and acquisition. The STM32F303K8 on the other hand is specifically designed for mixed-signal applications, with high-performance ADC and DAC peripherals, advanced timer capabilities and DMA support. However, it lacks support for wireless communication and has limited flash and RAM resources, making it unsuitable for complex user interfaces. Thus, a dual-microcontroller architecture was used.

The STM32 serves as the measurement subsystem, interfacing with the analogue frontend to perform measurements. Results are then sent to the ESP32 via UART. The ESP32 acts as the system controller, managing calibration, sending commands to the STM32 and handling the user interfaces. An on-device LCD with buttons provides an interface for standalone operation in any setting, while an optional web-based interface accessible via Bluetooth Low Energy (BLE) enables enhanced usability when client devices are available.
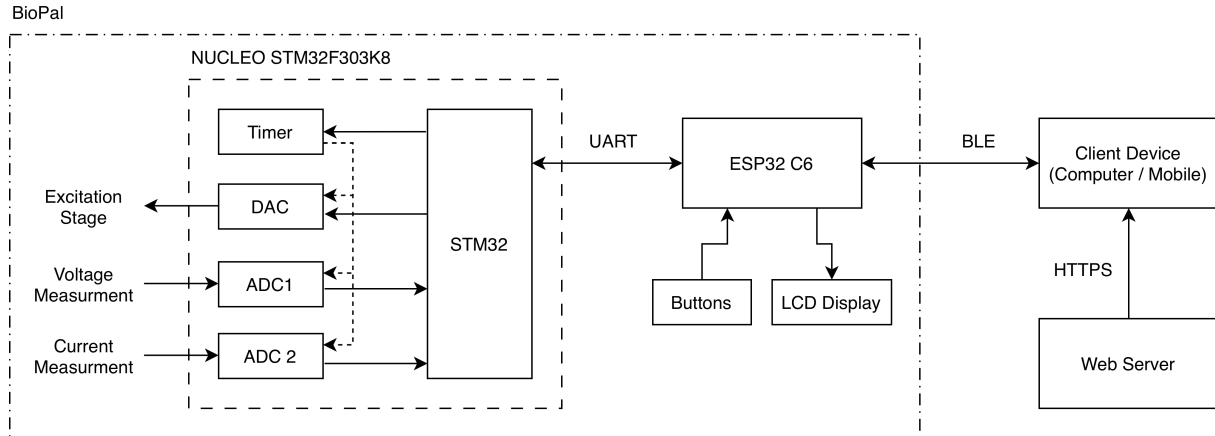
Figure 3.26: Embedded System Diagram

3.6.1. STM32 Measurement Subsystem

The STM32F303K8 includes a 12-bit DAC and 12-bit ADCs with up to 1 Msps sampling. Advanced timers enable precise frequency generation for the excitation stage with sub-microsecond accuracy. The ARM Cortex-M4F core includes a hardware floating point unit (FPU) and digital signal processing (DSP) extensions, providing native support for fast Fourier transform (FFT) operations through the CMSIS-DSP library.

DMA channels enable DAC output and simultaneous sampling of both ADCs without CPU intervention, ensuring precise phase measurements. The STM32 generates the excitation waveform, controls the multiplexer, PGA and TIA gain settings, acquires voltage and current measurements, performs digital filtering and FFT analysis, and transmits impedance results to the ESP32.

3.6.2. ESP32 User Interface and System Control

The ESP32-C6 serves as the system controller, accepting user inputs, sending measurement commands to the STM32, calibrating the resulting measurements and displaying results to the user. The larger flash and RAM resources on the ESP32 allowed for the use of Free RTOS,allowing for multitasking and improved system responsiveness. The ESP32 also handles the two user interfaces.

On-Device Interface

Physical buttons and an LCD display enable complete standalone operation. Combined with battery power, this ensures the device functions in any resource-constrained setting without requiring external hardware. The interface provides immediate feedback and control, critical for POC environments where reliable operation cannot depend on network connectivity or additional devices.

Web Interface via BLE

A secondary web-based interface provides enhanced usability when network-connected devices are available. Three implementation approaches were considered:

Option 1 - Existing WiFi Network: The device connects to an existing network, enabling control over WiFi or the internet. While convenient once configured, this approach poses significant barriers in healthcare environments with strict network security policies protecting patient data. It also excludes settings without WiFi infrastructure, such as rural clinics.

Option 2 - Device WiFi Hotspot: The device hosts its own WiFi network, serving a local website. This avoids secure network requirements and functions everywhere, but forces client devices offline, potentially disrupting other applications and services.

Option 3 - Web Application with BLE: A web application hosted remotely connects to the device via BLE. This approach was selected as it provides the benefits of both previous options without their drawbacks. Client devices maintain internet connectivity, no secure network authentication is required, and the solution works universally. Critically, all measurement data transfers locally over BLE, eliminating security risks and POPIA compliance concerns associated with transmitting patient information over the internet. The web-based implementation ensures cross-platform compatibility across mobile, desktop, and tablet devices regardless of operating system.

Communication between the ESP32 and STM32 occurs via UART, with a protocol designed for reliable transmission of measurement parameters, gain settings, and impedance results. The ESP32 polls the STM32 for measurement status and retrieves data once processing completes.

3.7. System Integration

Chapter 4

Testing & Validation

The testing and validation process was structured to systematically verify the functionality of the impedance analyser, progressing from subsystem verification to complete system integration and finally calibration and validation with actual biosensors. This methodical approach allowed for the identification and correction of issues at each stage, ensuring that problems could be isolated and resolved before integration with more complex subsystems.

4.1. PCB Testing

Upon receiving the assembled PCB visual inspection and continuity testing confirmed no obvious short circuits or discontinuities. The ESP32's onboard battery charging circuit was confirmed to supply a stable 3.3 V rail to all digital and analogue components. The virtual ground reference circuit was measured at exactly 1.650 V. The TPS61072 boost converter successfully provided a stable 5 V supply for the LTC1069 anti-aliasing filter.

Next, each subsystem was tested individually whilst other subsystems remained disconnected. This approach allowed for precise characterisation of each stage's performance and simplified fault diagnosis.

4.1.1. Excitation Stage

The excitation stage was tested using a signal generator providing a 3 Vpp input signal and an oscilloscope to measure the attenuated output. Unfortunately, the LTC1069 anti-aliasing filter was found to be dead-on-arrival. Given the significant lead times for component procurement and project time constraints, it was not feasible to order a replacement. The filter was therefore bypassed, and the excitation stage was tested without it. Whilst this introduces higher-frequency components from the DAC's stairstepping, the synchronisation of DAC generation and ADC sampling in the final system helps to minimise the impact on measurements.

The attenuation stage was characterised across the full frequency range from 1 Hz to 100 kHz. Measuring phase and exact magnitude at very small amplitudes proved difficult due to the ADC noise of the digital oscilloscope [37]. This meant that the resulting 10mVpp signal's phase and voltage had to be manually measured using cursors. The measured

attenuation was 300 V/V (or a gain of 0.0033 V/V), as designed. Figure 4.1 shows the frequency response, which exhibits a flat gain and phase across the measurement range.

Figure 4.1: Excitation Stage Frequency Response

4.1.2. Voltage Measurement Stage

The voltage measurement stage was tested in three configurations: the INA331 instrumentation amplifier alone (using a 10mVpp input), the TLV9061 gain stage alone (using a 150 mVpp input). The INA331 performed as expected, with no measurable gain roll-off at 100 kHz. However, the measured phase shift of -6.5° was slightly larger than the predicted -4.6°. This discrepancy likely arises from parasitic capacitances in the PCB layout and component tolerances that were not fully captured in the simulation model.

Initial testing of the TLV9061 stage showed a completely unstable system. Investigation uncovered a critical oversight in the PCB design: the TLV9061 op-amp symbol used in KiCad had a different pinout than the LTspice model used for simulation, resulting in the inverting and non-inverting inputs being swapped. This was corrected through careful trace cutting and wire jumpers, and the corrected schematic was updated in KiCad for future PCB revisions. After this modification, the TLV9061 stage performed well, exhibiting a -9° phase shift at 100 kHz compared to the expected -3.4°. The larger-than-expected phase shift can be attributed to several factors: the additional parasitic capacitance introduced by the rework, tolerances in the op-amp's gain-bandwidth product, and PCB layout effects not fully captured in simulation. The measured gain roll-off at 100 kHz was TBD dB. Overall, the voltage measurement stage's performance closely matched expectations, with the phase discrepancies remaining well within acceptable limits for accurate impedance measurements if properly calibrated for.

Table wat cutoff en 100kHz summarise vir elke afdeling en dan langs dit grafiek wat responses van elke substage wyse op eenm grafiek

4.1.3. Current Measurement Stage

The current measurement stage required the most extensive testing due to its complexity and switchable gain configurations. Significant concerns existed regarding the TIA functionality given the extremely small 0.4 mm pitch BGA package of the OPA3S328.

The TIA was characterised by applying known voltages across resistors of known values, allowing the input current to be calculated. The TIA output voltage was then measured to determine the transimpedance gain. Whilst the resistor values were measured using a standard multimeter and may have some tolerance-related uncertainty, this characterisation served primarily for functional validation, as final calibration would be performed against the PalmSens4.

At $R_f = 37.5\,\Omega$, the TIA exhibited a phase shift of TBD° and gain reduction of TBD dB at 100 kHz. At the larger feedback resistor value of $R_f = 7.5\,k\Omega$, both phase shift and gain reduction were more pronounced at TBD° and TBD dB respectively at 100 kHz. However, this higher gain setting is only used at lower frequencies where the biosensor impedance is very high. At 250 Hz, which represents the upper frequency limit for using $R_f = 7.5\,k\Omega$ in the measurement protocol, the phase shift and gain reduction were significantly lower at TBD° and TBD dB respectively.

Stability was verified by connecting a simplified Randles equivalent circuit with a constant double-layer capacitance approximating the expected biosensor characteristics. A 10 mVpp signal was swept from 1 Hz to 10 MHz while monitoring the TIA output for oscillations, ringing, or excessive peaking in the frequency response. No instability was observed, confirming the theoretical analysis in Section 3.3.3 that showed feedback compensation capacitors were unnecessary for biosensor TIA circuits due to the series resistance in the Randles equivalent circuit.

The PGA113 was measured at each gain setting from 1 V/V to 200 V/V. Table 4.1 shows the measured gain and phase shift at 100 kHz for each setting, demonstrating close agreement with the expected performance across the entire gain range.

Table 4.1: PGA113 Performance at 100 kHz

Gain Setting (V/V)	Expected Gain (V/V)	Measured Gain (V/V)	Expected Phase (°)	Measured Phase (°)
1	1.00	TBD	0.0	TBD
2	2.00	TBD	TBD	TBD
5	5.00	TBD	TBD	TBD
10	10.00	TBD	TBD	TBD
20	20.00	TBD	TBD	TBD
50	50.00	TBD	TBD	TBD
100	100.00	TBD	TBD	TBD
200	200.00	TBD	TBD	TBD

The final TLV9061 amplification stage in the current measurement path was modified using the same trace cutting and rewiring procedure as the voltage measurement stage. Measurements confirmed no measurable difference in performance compared to the voltage measurement path, ensuring that gain reductions and phase shifts cancel during impedance calculation as designed.

4.2. System Calibration

With all subsystems verified individually, the system was integrated and calibrated. The complete analogue frontend was tested using passive test cells, initially with a signal generator providing the excitation. Once analogue system stability and measurement accuracy were confirmed, the STM32 was used to generate DAC signals and acquire responses with the ADCs.

The STM32's ADCs were calibrated by applying a series of known voltages using a bench power supply, with each voltage verified using an oscilloscope and multimeter. The offset and gradient correction factors for each ADC channel were then determined. Similarly, the DAC output was measured, and the centre point of the generated signal adjusted from 2048 to 2009. This ensured that the analogue output was precisely centred at 1.65 V, ensuring the biosensor is not biased with a DC voltage.

The DAC's frequency generation capability was verified by measuring the output waveform at each test frequency from 1 Hz to 100 kHz using an oscilloscope. Frequency was confirmed to be accurate across the entire range, validating the timer configuration and DMA-based waveform generation. However, some very slight low frequency, frequency modulation was observed.

Initial calibration attempts using precision resistors measured with the PalmSens4 across the full frequency range (to account for parasitic impedances) proved problematic. Each TIA and PGA gain combination was calibrated separately using these measurements. However, when testing Randles equivalent circuits or actual biosensors, the frequency-dependent impedance characteristics resulted in unacceptably large error margins. The fixed PGA gain used during calibration did not match the actual measurement conditions, where gain settings vary with frequency to maintain optimal ADC range utilisation.

This led to a revised calibration approach. The gain settings for each frequency were pre-programmed to match the expected impedance range at that frequency based on PalmSens4 characterisation of the biosensors. A non-faradaic Randles equivalent test cell was then measured simultaneously with both the BioPal and the PalmSens4, and the BioPal's response was calibrated against the PalmSens4 measurements. This approach accounts for the complete signal chain at the actual gain settings used during biosensor measurements, significantly improving accuracy.

4.3. Biosensor Validation

The final validation stage involved measurements on actual biosensors using phosphate buffered saline (PBS) solution and bovine serum albumin (BSA) protein. PBS 1× was selected as the electrolyte solution due to its physiological ionic strength and pH (7.4), which closely mimics the conditions in bodily fluids and provides a stable, well-characterised

electrochemical environment for biosensor operation.

Figure 4.2 shows impedance measurements of the biosensor in different PBS concentrations, demonstrating the BioPal's ability to clearly distinguish between solution conductivities. The impedance magnitude decreases with increasing PBS concentration as expected, confirming the device's sensitivity to electrochemical changes.

Figure 4.2: Biosensor Impedance Response to Different PBS Concentrations

Whilst testing with immobilised antibodies and actual protein antigens would provide the most direct validation of biosensing capability, such tests were beyond the scope of this project due to laboratory safety restrictions, cost constraints, and limited time. Instead, BSA was used as a surface-binding protein to simulate antibody-antigen interactions. BSA is a common blocking protein that readily adsorbs to gold electrode surfaces, creating a protein layer that alters the interfacial impedance characteristics. This mimics the effect of antibody-antigen binding on the electrode surface, allowing validation of the device's ability to detect surface-based electrochemical changes rather than bulk solution properties.

The measurement protocol involved establishing a baseline impedance measurement in PBS 1×, adding BSA solution to the electrode well, allowing 20 minutes for protein adsorption, flushing the electrode three times with fresh PBS 1× to remove unbound protein whilst maintaining the same solution characteristics, and finally performing a second impedance measurement. This approach isolated the impedance change due to surface modification from any changes in bulk solution properties.

Measurements were performed simultaneously using both the BioPal and the PalmSens4 for direct comparison. Figure 4.3 shows the impedance magnitude and phase measurements from both instruments before and after BSA binding. The BioPal successfully detected the impedance increase following BSA adsorption, demonstrating its capability to measure surface-based electrochemical changes relevant to biosensing applications.

(a) Impedance Magnitude   **(b)** Phase

Figure 4.3: Comparison of BioPal and PalmSens4 Measurements Before and After BSA Binding

4.4. Discussion of Results

The BioPal's performance varied across the measurement frequency range, with distinct regions of accuracy. At very low frequencies (below X Hz), the biosensor impedance becomes extremely high, resulting in currents in the tens of nanoamperes. At these current levels, the signal-to-noise ratio decreases substantially, making it difficult to distinguish

the frequency content of interest from background noise. Consequently, measurements in this region exhibited large error margins. However, the overall trend still aligned with PalmSens4 measurements, indicating that whilst absolute accuracy was compromised, the relative changes were correctly captured.

At slightly higher frequencies (X Hz to X Hz), measurement accuracy improved dramatically as current levels increased and the signal-to-noise ratio became more favourable. Error margins reduced substantially, though some discrepancy from the PalmSens4 remained visible. The optimal measurement range was found to be X Hz to X Hz, where error margins were minimal and measurements closely tracked the reference instrument. This frequency range aligns well with the region where surface characteristic changes are most prominent in EIS biosensing, making it particularly relevant for detecting analyte binding events. These are the frequencies where changes in the double-layer capacitance and charge transfer resistance due to biomolecular interactions at the electrode surface are most readily observable.

At very high frequencies (above X Hz), error margins increased slightly again. This can be attributed to several factors: the phase shifts in the measurement circuitry become more significant, the absence of the anti-aliasing filter allows more high-frequency noise into the system, and the parasitic capacitances and inductances in the PCB layout begin to affect measurements more noticeably.

Despite these frequency-dependent variations in accuracy, the BioPal successfully demonstrated its core capability: detecting and quantifying impedance changes at key frequencies relevant to biosensing. The device clearly distinguished between baseline and post-BSA measurements, identifying the characteristic impedance increase associated with protein binding to the electrode surface. This validates the BioPal's applicability for quantitative biosensor measurements in point-of-care settings.

The results demonstrate that the BioPal can provide point-of-care healthcare professionals with a low-cost, portable tool for rapid disease screening. Whilst it does not match the precision of laboratory-grade instruments like the PalmSens4 across the entire frequency spectrum, it performs well in the critical frequency ranges for biosensor applications. This enables healthcare workers to quickly screen patients and identify individuals who require further testing or specialist referral, without the need for expensive laboratory equipment or extensive technical training. The device thus fulfils its design objective of democratising biosensor-based diagnostics for resource-limited settings.

Chapter 5

Summary and Conclusion

Bibliography

[1] L. Chioye, "Build a Programmable Gain Transimpedance Amplifier Using the OPA3S328," 2021.

[2] "Stabilize Your Transimpedance Amplifier | Analog Devices," https://www.analog.com/en/resources/technical-articles/stabilize-transimpedance-amplifier-circuit-design.html.

[3] "Sboa311a."

[4] N. Bhalla, P. Jolly, N. Formisano, and P. Estrela, "Introduction to biosensors," *Essays in Biochemistry*, vol. 60, no. 1, pp. 1–1, Jun. 2016.

[5] "Biomarkers | National Institute of Environmental Health Sciences."

[6] A. Rosenzweig, "What Are Pancreatic Cancer Biomarkers? - Pancreatic Cancer Action Network," 2018.

[7] J. A. Ribeiro and P. A. Jorge, "Applications of electrochemical impedance spectroscopy in disease diagnosis—A review," *Sensors and Actuators Reports*, vol. 8, pp. 100 205–100 205, Dec. 2024.

[8] X. Zeng, Z. Shen, and R. Mernaugh, "Recombinant antibodies and their use in biosensors," *Analytical and bioanalytical chemistry*, vol. 402, no. 10, pp. 3027–3038, Apr. 2012.

[9] S. Sueda, "Antibody immobilization for immunosensing," *Analytical Sciences*, vol. 38, no. 1, pp. 1–2, Jan. 2022.

[10] "Using Antibodies as vaccine delivery vehicles," https://downhousesoftware.wordpress.com/2013/12/.

[11] J. S. Daniels and N. Pourmand, "Label-Free Impedance Biosensors: Opportunities and Challenges," *Electroanalysis*, vol. 19, no. 12, pp. 1239–1257, 2007.

[12] H. S. Magar, R. Y. A. Hassan, and A. Mulchandani, "Electrochemical Impedance Spectroscopy (EIS): Principles, Construction, and Biosensing Applications," *Sensors*, vol. 21, no. 19, p. 6578, Jan. 2021.

[13] A. C. Lazanas and M. I. Prodromidis, "Erratum: Electrochemical Impedance Spectroscopy-A Tutorial (ACS Measurement Science Au (2023) 3:3 (162-193) DOI: 10.1021/acsmeasuresciau.2c00070)," *ACS Measurement Science Au*, vol. 2023, no. 3, pp. 14–14, 2025.

[14] "EIS Quality Indicators and Linearity Correction."

[15] Q.-Z. Xie, M.-W. Lin, E.-W. Hsu, and C.-T. Lin, "Review—Advancements of Nanoscale Structures and Materials in Impedimetric Biosensing Technologies," *ECS Journal of Solid State Science and Technology*, vol. 9, p. 115027, Oct. 2020.

[16] "Bode and Nyquist Plot."

[17] L. A. Buscaglia, J. P. Carmo, and O. N. Oliveira, "Simple-Z: A Low-Cost Portable Impedance Analyzer," *IEEE Sensors Journal*, vol. 23, no. 21, pp. 26 067–26 074, Nov. 2023.

[18] A. Al-Ali, A. Elwakil, A. Ahmad, and B. Maundy, "Design of a Portable Low-Cost Impedance Analyzer," *BIODEVICES 2017 - 10th International Conference on Biomedical Electronics and Devices, Proceedings; Part of 10th International Joint Conference on Biomedical Engineering Systems and Technologies, BIOSTEC 2017*, vol. 2, pp. 104–109, Feb. 2017.

[19] M. Ibrahim, "CMOS Transimpedance Amplifier for Biosensor Signal Acquisition."

[20] ""Improved" Howland current pump circuit," 2020.

[21] L. Gaddy and H. Kawai, "DYNAMIC PERFORMANCE TESTING OF DIGITAL AUDIO D/A CONVERTERS."

[22] e. technology, "What are the Drawbacks of Differential Amplifier Circuits?" https://www.eimtechnology.com/blogs/articles/what-are-the-drawbacks-of-differential-amplifier-circuits, Apr. 2024.

[23] "The Instrumentation Amplifier | Operational Amplifiers | Electronics Textbook," https://www.allaboutcircuits.com/textbook/semiconductors/chpt-8/the-instrumentation-amplifier/.

[24] T. Brown, "Design Thinking," *Harvard Business Review*, Jul. 2008.

[25] "PalmSens4," https://www.palmsens.com/product/palmsens4/.

[26] T. Ebrahim, "The development of a biosensor for the early detection of pancreatic cancer," 2023.

[27] C. Dincer, R. Bruch, A. Kling, P. S. Dittrich, and G. A. Urban, "Multiplexed Point-of-Care Testing – xPOCT," *Trends in Biotechnology*, vol. 35, no. 8, pp. 728–742, Aug. 2017.

[28] "LTC1069-7CS8#PBF," https://www.digikey.co.za/en/products/detail/analog-devices-inc/LTC1069-7CS8-PBF/889060.

[29] J. M. Fiore, "5.3: Gain-Bandwidth Product," in *Operational Amplifiers and Linear Integrated Circuits - Theory and Application (Fiore)*, May 2018.

[30] M. Oljaca and H. Surtihadi, "Operational amplifier gain stability, Part 1: General system analysis," 2010.

[31] "Selecting the Right CMOS Analog Switch | Analog Devices," https://www.analog.com/en/resources/design-notes/selecting-the-right-cmos-analog-switch.html.

[32] "WEBENCH-CIRCUIT-DESIGNER Design tool | TI.com," https://www.ti.com/tool/WEBENCH-CIRCUIT-DESIGNER.

[33] M. Wilson, L. Cowie, V. Farrow, M. Cree, and J. Scott, *Simulating Fractional Capacitors with the SPICE Circuit Simulator*, Sep. 2023.

[34] "Filter manual," http://ltspicegoodies.ltwiki.org/FilterManual.php#FIR_examples.

[35] "PGA113 Pspice model - Logic forum - Logic - TI E2E support forums," https://e2e.ti.com/support/logic-group/logic/f/logic-forum/1178762/pga113-pspice-model, Dec. 2022.

[36] "What Are the Basic Guidelines for Layout Design of Mixed-Signal PCBs? | Analog Devices," https://www.analog.com/en/resources/analog-dialogue/articles/what-are-the-basic-guidelines-for-layout-design-of-mixed-signal-pcbs.html.

[37] "I'm seeing unexpected noise on my ocsilloscope." https://www.tek.com/en/support/faqs/im-seeing-unexpected-noise-my-ocsilloscope.

Appendix A

Project Planning Schedule

This is an appendix.

Appendix B

Outcomes Compliance

This is another appendix.